

A brown dwarf donor and an optically thin accretion disc with a complex stream impact region in the period-bouncer candidate BW Sculptoris

Vitaly V. Neustroev^{1*}, Iikka Mäntynen^{1,2}

¹*Space Physics and Astronomy research unit, PO Box 3000, FI-90014 University of Oulu, Finland*

²*Department of Physics and Astronomy, University of Turku, FI-20014 Turku, Finland*

Accepted 2023 June 5. Received 2023 June 4; in original form 2022 August 23

ABSTRACT

We present an analysis of multi-epoch spectroscopic and photometric observations of the WZ Sge-type dwarf nova BW Scl, a period-bouncer candidate. We detected multiple irradiation-induced emission lines from the donor star allowing the radial velocity variations to be measured with high accuracy. Also, using the absorption lines Mg II 4481 Å and Ca II K originated in the photosphere of the accreting white dwarf (WD), we measured the radial velocity semi-amplitude of the WD and its gravitational redshift. We find that the WD has a mass of $0.85 \pm 0.04 M_{\odot}$, while the donor is a low-mass object with a mass of $0.051 \pm 0.006 M_{\odot}$, well below the hydrogen-burning limit. Using NIR data, we put an upper limit on the effective temperature of the donor to be ≤ 1600 K, corresponding to a brown dwarf of T spectral type. The optically thin accretion disc in BW Scl has a very low luminosity $\lesssim 4 \times 10^{30}$ erg s^{−1} which corresponds to a very low-mass accretion rate of $\lesssim 7 \times 10^{-13} M_{\odot}$ yr^{−1}. The outer parts of the disc have a low density allowing the stream to flow down to the inner disc regions. The brightest part of the hotspot is located close to the circularization radius of the disc. The hotspot is optically thick and has a complex elongated structure. Based on the measured system parameters, we discuss the evolutionary status of the system.

Key words: binaries: close – stars: evolution – stars: individual: BW Scl – novae, cataclysmic variables.

1 INTRODUCTION

Cataclysmic variables (CVs) are interacting binaries in which the primary, a white dwarf (WD) accretes matter from the secondary, a late-type donor star (Warner 1995). The standard evolution of CVs is driven by angular momentum loss, which results in CVs evolving from longer orbital periods to shorter ones before reaching a minimum period of $P_{\min} \approx 70$ –80 min (Kolb 1993; Howell et al. 1997, 2001; Knigge et al. 2011; Belloni et al. 2020). Approaching P_{\min} , the donor star evolves into a sub-stellar, brown dwarf-like object, at which point the orbital period P_{orb} of the binary starts increasing again. CVs that have passed beyond P_{\min} and are bouncing back towards longer periods are called ‘period bouncers’.

Population models predict a vast number of highly evolved CVs with sub-stellar donors (up to 80% of the present day Galactic CV population – Belloni et al. 2020; see also Kolb 1993; Goliasch & Nelson 2015; Schreiber et al. 2016), whereas only about two dozens of more or less robust candidates for these predicted objects have been identified until now (for published compilations see Patterson 2011; Kimura et al. 2018). Moreover, direct (spectral) evidence for brown dwarf donors exists only for very few CVs (SDSS J143317.78+101123.3; Hernández Santisteban et al. 2016; WZ Sge; Harrison 2016, 2017; SDSS J123813.73−033933.0; Pala et al. 2019). The recognition of the sub-stellar nature of the donors in other period-bounce candidates is based on indirect methods such as radial

velocity measurements of the WDs, the use of a superhump period–mass ratio relation and analysis of the spectral energy distribution (SED).

An accurate characterization of donor stars in old CVs is a challenging task because the donor photometric properties along the CV evolution sequence change dramatically. In period bouncers, a brown dwarf donor of very late spectral type (L/T) is expected (Knigge et al. 2011). Such a donor star is so dim that even a weak contribution from the accretion disc and the accretion-heated WD can easily outshine it. Littlefair et al. (2003) suggest that the chances of detecting the brown dwarf donors are increased in nearby CVs with little or no ongoing accretion.

BW Sculptoris, a ~ 16.5 mag blue star, is one of the brightest and closest CVs ($d = 93.3 \pm 0.4$ pc – Gaia Collaboration et al. 2021; Bailer-Jones et al. 2021) included to the period-bouncer scorecard by Patterson (2011). It was discovered as a soft X-ray source in the ROSAT all-sky survey (RX J2353.0−3852; Abbott et al. 1997) and independently found in Hamburg/ESO survey for bright quasars (HE 2350−3908; Augusteijn & Wisotzki 1997). These two studies established that BW Scl is a CV with the very short orbital period of ~ 78.2 min, the shortest known to that date. Photometric observations performed by Uthas et al. (2012) from 1999 to 2009 resulted in an accurate measurement of the orbital period $P_{\text{orb}} = 78.22639 \pm 0.00003$ min. In addition to double-peaked emission lines, the spectrum of BW Scl also shows very broad Lyman and Balmer absorption lines from the underlying accreting WD of modest temperature (~ 15000 K – Gänsicke et al. 2005; Pala et al. 2022). Such a spectrum was found to be very similar to WZ Sge, which

* E-mail: vitaly@neustroev.net

Table 1. Log of spectroscopic observations of BW Scl.

HJD-Start 2450000+	Telescope / Instrument	Sp. res R	λ range (Å)	Exp.time (s)	Number of exps.	Duration (h / P_{orb})
2227.4977	VLT / UVES	44000	4020–5245	300	60	5.53 / 4.24
2228.5051	VLT / UVES	44000	3300–4520	300	15	1.30 / 1.00
2228.5057	VLT / UVES	44000	4625–5600	300	15	1.30 / 1.00
2228.5057	VLT / UVES	46000	5680–6650	300	15	1.30 / 1.00
2228.5643	VLT / UVES	44000	4020–5245	300	30	2.68 / 2.05
2494.7781	VLT / UVES	44000	4020–5245	300	34	4.15 / 2.41
2495.8042	VLT / UVES	44000	4020–5245	300	8	0.68 / 0.52
5482.4935	VLT / X-shooter	4300	3000–5560	60	239	5.54 / 4.25
5482.4935	VLT / X-shooter	7400	5560–10200	60	239	5.54 / 4.25
5482.4935	VLT / X-shooter	5400	9950–24780	60	239	5.54 / 4.25
8030.5847	NTT / SOFI	1000	9500–16400	180	26	1.32 / 1.01
8385.6834	NTT / EFOSC2	800	3300–5200	300	1	0.08 / 0.06
8385.6868	NTT / EFOSC2	1000	4700–6770	180	22	1.30 / 1.00
8385.7422	NTT / EFOSC2	600	4045–7445	300	1	0.08 / 0.06

allowed [Augustejn & Wisotzki \(1997\)](#) to argue that the source is a dwarf nova with a long recurrence time and a very low mass-transfer rate. This motivated [Mennickent et al. \(2004\)](#) to conduct a search for a brown dwarf in BW Scl, but near-infrared (NIR) spectroscopy has failed to reveal the donor in this system.

In October 2011, BW Scl experienced a superoutburst of an amplitude of ~ 7.5 mag ([Kato et al. 2013](#)), confirming thus a WZ Sge-type classification (for a review of the WZ Sge-type dwarf novae, see [Kato 2015](#)). Based on their method of estimating binary’s mass ratios by using the period of superhumps, [Kato & Osaki \(2013\)](#) reported a mass ratio of BW Scl to be $q \equiv M_2/M_{\text{WD}} = 0.067 \pm 0.006$, where M_2 and M_{WD} are masses of the donor and the WD, respectively. An even lower mass ratio ($q = 0.062$) can be obtained from another empirical relation between q and the orbital and superhump periods ([McAllister et al. 2019](#)). Together with a mass estimate for the WD of $1.01 M_{\odot}$ derived by [Pala et al. \(2022\)](#) from the re-analysis of the *Hubble Space Telescope* (HST) data ([Gänsicke et al. 2005](#)), this yields the donor mass to be $0.062\text{--}0.068 M_{\odot}$. This mass range does not allow for a certain confirmation of the donor’s brown dwarf status because it is only slightly lower than the hydrogen-burning mass limit ([Kumar 1963](#); [Hayashi & Nakano 1963](#)). Still, these estimates are based on indirect estimates from relations which are not well calibrated at very low-mass ratios.

This motivated us to perform a detailed spectroscopic study of BW Scl aiming in a more reliable determination of the fundamental system parameters. As a result, we confirm the sub-stellar nature of the donor star and argue that BW Scl has already passed the minimum period and is now evolving back towards longer periods.

2 THE DATA

The quantitative analysis presented in this work is based primarily on the spectra obtained with different telescopes and instruments of the European Southern Observatory (ESO). The full journal of spectroscopic observations is presented in [Table 1](#). These data combine new and archival material. The new observations are photometry and spectroscopy taken with the New Technology Telescope (NTT) at La Silla Observatory (Chile). We complement our observations with archival spectroscopic data which were obtained with the Very Large Telescope (VLT) at the Paranal Observatory in Chile, using the medium resolution spectrograph X-shooter and the Ultraviolet

and Visual Échelle Spectrograph (UVES). See [Section 2.1](#) for more detail regarding these data.

Our data sets also comprise new observation of BW Scl with the Neil Gehrels Swift Observatory ([Section 2.2](#)). Additionally, we employed high-level science products derived from some other archives, which we describe in due course.

2.1 Optical and NIR photometry and spectroscopy

We used the NTT telescope to perform multicolour optical and NIR photometry and spectroscopy of BW Scl (programs 100.D-0932 and 101.D-0806; PI: V. Neustroev). The NIR observations were made on 2017 October 4 with the infrared spectrograph and imaging camera SOFI ([Moorwood et al. 1998](#)) mounted at the Nasmyth A focus of the NTT. The NIR images were obtained through the JHK_s filters, while the spectra were taken with the blue grism covering the wavelength range 9500–16400 Å. The data were taken under clear atmospheric conditions with seeing ~ 1 arcsec. In order to increase the resolving power to about $R \sim 1000$, we used a narrow slit of 0.6 arcsec. Spectra of the telluric standard Hip 117513 were taken before and after the observations of the target for flux calibrations. A comparison spectrum of a xenon lamp was used for wavelength calibration. The SOFI data were reduced using the PESSTO pipeline version 2.4.1 ([Smartt et al. 2015](#)).

The optical data were acquired with the ESO Faint Object Spectrograph and Camera EFOSC2 ([Buzzoni et al. 1984](#)) mounted at the Nasmyth B focus of the NTT. The images were captured on 2017 October 5 through the BVRiz filters. The spectroscopic observations were performed on 2018 September 24 under perfect weather conditions with seeing 0.6–0.7 arcsec, allowing us to use a narrow slit of 0.7 arcsec. The time-resolved observations were taken with grism #18 in the wavelength range of 4700–6770 Å with a spectral resolution of 5.7 Å. A total of 22 spectra with 180 s individual exposures were obtained, covering one orbital period of the system. In order to maximize the wavelength coverage, we also took two additional spectra using grisms #4 and #7 with the exposure times of 300 s, providing an overall wavelength coverage of 3270–7520 Å. For flux calibrations, spectra of the standard spectrophotometric star LTT 7987 were taken. For wavelength calibrations, He-Ar lamp exposures were obtained. The EFOSC2 data were reduced using IRAF package in a standard way.

The optical magnitudes of BW Scl in different filters were measured using four comparison stars in the field. Their magnitudes were obtained from the VST ATLAS survey¹ (Shanks et al. 2015), DR4 data release. The NIR magnitudes were calibrated using the same comparison stars as were chosen for the optical photometry. Their magnitudes and errors were taken from the 2MASS All-Sky Catalog of Point Sources (Cutri et al. 2003). The derived magnitudes of BW Scl are shown in Table 2. In the following, we call the data which were obtained with the NTT as the NTT data set, or the EFOSC2 or SOFI spectra if necessary.

BW Scl was observed twice with VLT/UVES (Dekker et al. 2000) in 2001 and 2002. The observations obtained on 2001 November 13–15 under program 068.D-0153 were performed using different configurations allowing to cover the wavelength range from 3300 to 6650 Å. All segments of the spectrum cover at least 1 orbital period of the system, while blue-arm spectra (4020–5245 Å) cover $\sim 6.3 P_{\text{orb}}$. The data taken on 2002 August 08–09 under program 069.D-0391 consist of only blue-arm spectra covering $\sim 2.9 P_{\text{orb}}$. All the UVES observations were acquired using a 0.9 arcsec slit yielding a resolving power of approximately 44000. An exposure time was 300 s. These data are referred to as the UVES data set, or the UVES-1 or UVES-2 spectra in case it is necessary to specify which observations (either obtained in 2001 or 2002) are used.

On 2010 October 12–13, BW Scl was also observed with the medium resolution spectrograph X-shooter (program ID 086.D-0775). This instrument is comprised of three detectors (Vernet et al. 2011): the UVB arm, covering 3000–5500 Å; the VIS arm, covering 5500–10000 Å; the NIR arm, covering 10000–25000 Å. The observations used slit widths of 1.0 arcsec, 0.9 arcsec and 0.9 arcsec for the UVB, VIS, and NIR arms, respectively, and 2×2 binning in the UVB and VIS arms. This resulted in a resolving power of 4300, 7400, and 5400 in the UVB, VIS, and NIR arms, respectively. A total of 239 spectra with 60 s individual exposures were obtained, covering ~ 4.2 orbital periods of the system. The observations were performed in STARE mode. We call this data set the X-shooter data, or the UVB, VIS, or NIR spectra.

The raw UVES and X-shooter data together with calibration files were retrieved from the ESO Science Archive Facility and reduced using the standard pipelines (UVES Workflow For Point Source Echelle Data version 6.1.6, and X-shooter Workflow for Physical Mode Data Reduction version 3.5.0) within ESO REFLEX version 2.11.5 (Freudling et al. 2013). The standard recipes were used to optimally extract and wavelength and flux calibrate each spectrum. Individual X-shooter VIS and NIR spectra were separately corrected for telluric absorption using MOLECFIT (Smette et al. 2015; Kausch et al. 2015). Finally, the wavelength scale of all the spectra of each data set was also barycentrically corrected.

In addition to individual spectra, we also produced flux-calibrated average spectra, which are a combination of all spectra from the corresponding data sets, uncorrected for orbital motion.² Because the obtained mean spectra can suffer from imperfect flux calibration,³ we scaled them to match the fluxes derived from either quasi-

simultaneous multicolour photometry (the NTT data) or acquisition images (the X-shooter data). Unfortunately, no acquisition images are available for the UVES data. Nevertheless, we show in Section 3.2 that during the UVES and X-shooter observations BW Scl was at nearly the same flux level. Since most of our mean spectra span a broad wavelength range, which is covered by several photometric passbands, we also attempted to correct the spectra for wavelength-dependent effects such as atmospheric transmission. For this, we followed an approach similar to that used e.g. by Larsen & Richtler (2006). The mean spectra were convolved with the filter bandpasses to determine the ratios of the photometric fluxes in each filter to the fluxes measured in the spectra. The ratios were then fitted by a low-order polynomial to establish a correction function. As a result, we have reached the flux calibration to be accurate within a few per cent in the whole wavelength range.⁴ Finally, BW Scl is a nearby source and its interstellar extinction of $E_{B-V} = 0.002 \pm 0.015$ (Lallement et al. 2018) is negligible for the analysis presented here (see Pala et al. 2017), thus no dereddening correction was applied.

2.2 X-rays and UV data

On 2021 April 06 we performed a 1.5 ks observation of BW Scl with the Neil Gehrels Swift Observatory (Gehrels et al. 2004), using both the X-ray Telescope (XRT; Burrows et al. 2005) and the UV/Optical Telescope (UVOT; Roming et al. 2005). The data were reduced and analysed using HEASOFT 6.28, together with the most recent version of the calibration files. The UVOT observation was carried out in all six available filters.

Swift-XRT detected a weak X-ray source with a count-rate of 0.023 ± 0.004 counts s^{-1} . The spectrum consists of only 35 counts; therefore, no meaningful spectral analysis is possible. To estimate the X-ray flux of BW Scl, we assumed that its spectrum is similar to other WZ Sge-type stars such as GW Lib and SSS J122221.7-311525 (Neustroev et al. 2018b). By using the count-rate as the scale factor, we obtain the unabsorbed X-ray flux of BW Scl in the 0.3–10 keV energy range to be $\sim 7.8 \times 10^{-13}$ erg $\text{cm}^{-2} \text{s}^{-1}$. A formal fit of the spectrum with an optically thin emission component (the APEC model in XSPEC), absorbed by a variable column gives a consistent estimate of the unabsorbed X-ray flux to be $(8.3 \pm 1.6) \times 10^{-13}$ erg $\text{cm}^{-2} \text{s}^{-1}$. This corresponds to the unabsorbed X-ray luminosity of $(8.6 \pm 1.7) \times 10^{29}$ erg s^{-1} , which is in agreement with the luminosities found for other WZ Sge-type stars in quiescence (Reis et al. 2013; Neustroev et al. 2018b).

In order to extend the wavelength coverage of BW Scl for our analysis, we have extracted the UV data obtained by the HST and the Galaxy Evolution Explorer (GALEX) satellite. Far-UV echelle spectroscopy was obtained with the Space Telescope Imaging Spectrograph (STIS) aboard HST in 1999 (for detail, see Gänsicke et al. 2005). We retrieved the spectrum covering the wavelength range of 1150–1710 Å from the StarCAT catalogue (Ayres 2010). GALEX has observed BW Scl over five separate visits in the NUV (1 in 2003 and 4 in 2005) and four visits in the FUV (1 in 2003 and 3 in 2005). We used the gPhoton package version 1.28.9 (Million et al. 2016) to extract the magnitudes from these observations.

¹ <https://astro.dur.ac.uk/Cosmology/vstatlas/>

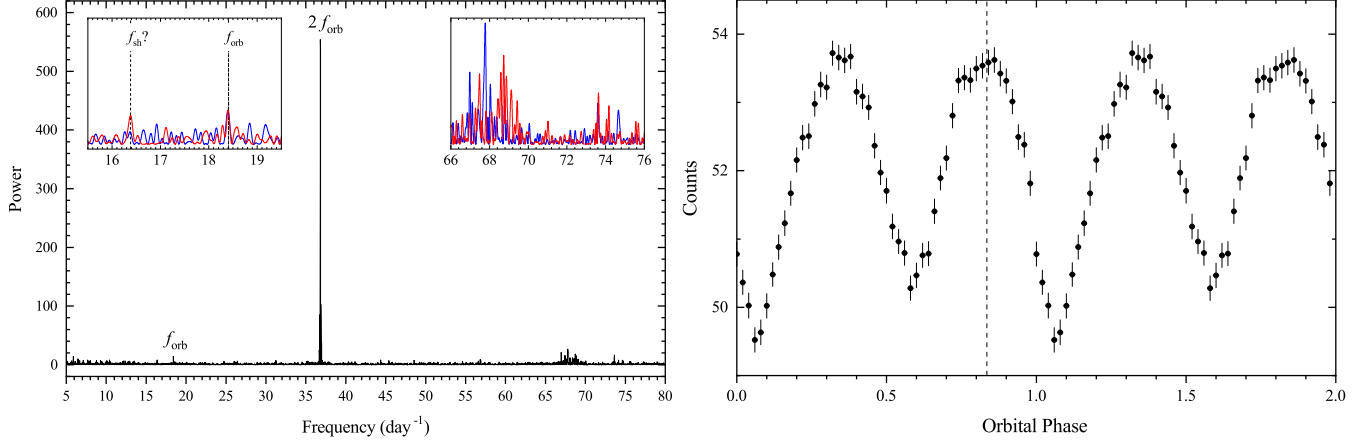
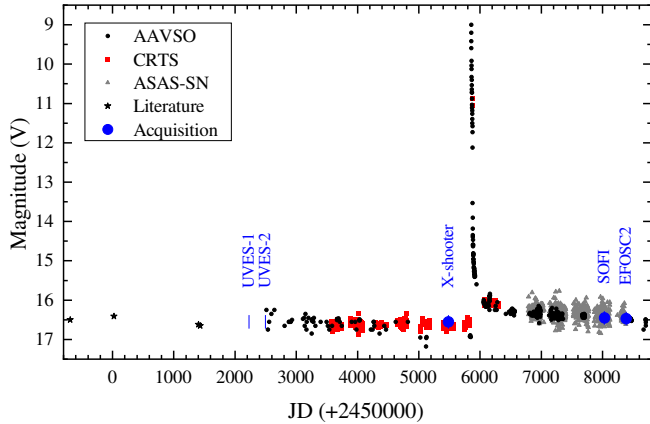
² The average X-shooter spectra were obtained by means of coadding science frames acquired within the same Observation Block (OB) before reducing them (the rule xsh_wkf_starestack.oca in ESO REFLEX). This approach was especially useful for the NIR arm, because the individual NIR spectra have a very low signal-to-noise ratio (SNR) ~ 1 in continuum.

³ A flux calibration method based on observations of spectrophotometric standards is subject of uncertainties due to slit losses and differences in seeing and weather conditions between observations of the target and standards.

⁴ Note that although the mean UVES-2 spectrum has a relatively high SNR of ~ 100 in continuum, it clearly shows the Échelle order pattern (Figure A1). Korn et al. (2007) pointed out that the blaze removal and order merging as implemented in the UVES pipeline leave significant residuals which may affect the analysis of WD lines.

Table 2. The magnitudes of BW Scl derived from the NTT and *Swift*-UVOT observations. They are given in the Vega system except for the *i* and *z* magnitudes which are in the AB system.

<i>uvw2</i>	<i>uvm2</i>	<i>uvw1</i>	<i>u</i>	<i>B</i>	<i>V</i>	<i>R_c</i>	<i>i</i>	<i>z</i>	<i>J</i>	<i>H</i>	<i>K_s</i>
14.97(2)	15.02(4)	15.22(4)	15.55(4)	16.60(3)	16.61(3)	16.37(1)	16.64(3)	16.97(3)	16.08(6)	15.76(6)	15.28(7)

**Figure 1.** Left: Lomb-Scargle power spectrum of the *TESS* photometry of BW Scl. The inset plots show the enlarged regions around the orbital and 66–76 cycle d^{-1} frequencies, in which [Uthas et al. \(2012\)](#) have detected transient signals. The blue and red lines in the insets correspond to the power spectra calculated for the *TESS* data obtained before and after the gap, respectively. Right: the *TESS* light curve folded with the P_{orb} according to spectroscopic ephemeris (2) and averaged in 50 phase bins. The dashed line indicates phase zero according to photometric ephemeris (1).**Figure 2.** Light curve of BW Scl combined of AAVSO, CRTS, and ASAS-SN observations from 1993 up to 2019. Also shown are measurements found in the literature ([Abbott et al. 1997](#); [Augusteijn & Wisotzki 1997](#); [Uthas et al. 2012](#); [Gänsicke et al. 2005](#)). The large blue dots represent averaged magnitudes of the object during our observations.

3 PHOTOMETRIC VARIABILITY OF BW SCL

3.1 Short-term variability

BW Scl in quiescence is known to exhibit short-term photometric variability with typical amplitude of ~ 0.1 mag ([Uthas et al. 2012](#)). Its light curve is dominated by cyclic modulations at half the orbital period ([Augusteijn & Wisotzki 1997](#)), for which [Uthas et al. \(2012\)](#) presented an ephemeris based on photometric observations from the years 1995–2009. The ephemeris is thus covering not only the UVES and X-shooter observations, but is also expected to be valid

for our NTT data. Indeed, Doppler maps which utilize these data and calculated according to the period from [Uthas et al. \(2012\)](#) exhibit no obvious phase difference (see Section 6.3). However, phase zero of the ephemeris causes confusion. According to [Uthas et al. \(2012\)](#), it corresponds to “orbital maximum”, whereas phase zero in their figure 6 corresponds to one of the (not deepest) light minima.

BW Scl was observed with the *Transiting Exoplanet Survey Satellite* (*TESS*) from 2020 August 26 to September 20 in Sector 29 at 20 second cadence. These observations provide the opportunity to obtain a long continuous coverage to test the stability of double-humped modulations in BW Scl, to resolve the confusion regarding phase zero, and to study other variabilities. We downloaded the *TESS* data in the Pre-search Data Conditioning Simple Aperture Photometry flux (PDCSAP) format from the Mikulski Archive for Space Telescopes (MAST) archive. In the PDCSAP light curves, instrumental systematic variations have been removed from the data in the pipeline reduction procedure. The light curve has a gap between 2020 September 6.23–9.83 (UT).

We calculated Lomb-Scargle periodograms for the total light curve ([Figure 1](#), left-hand panel), and separately for its two pieces consisting of the data obtained before and after the gap. The periodograms are exclusively dominated by a very strong and sharp peak at half the orbital frequency of $36.816 \pm 0.015 \text{ d}^{-1}$, consistent with the findings of [Uthas et al. \(2012\)](#), although a signal at the orbital frequency is also clearly present. [Figure 1](#) (right-hand panel) shows the *TESS* light curves folded with the orbital period and averaged in 50 phase bins. The folded light curve exhibits double-humped modulations with a total amplitude of ~ 0.08 mag and a small even-odd asymmetry. Attempting to improve the ephemeris, we combined the *TESS* data with the observations from the AAVSO (American Association of Variable Star Observers) obtained in 2002–2020, and

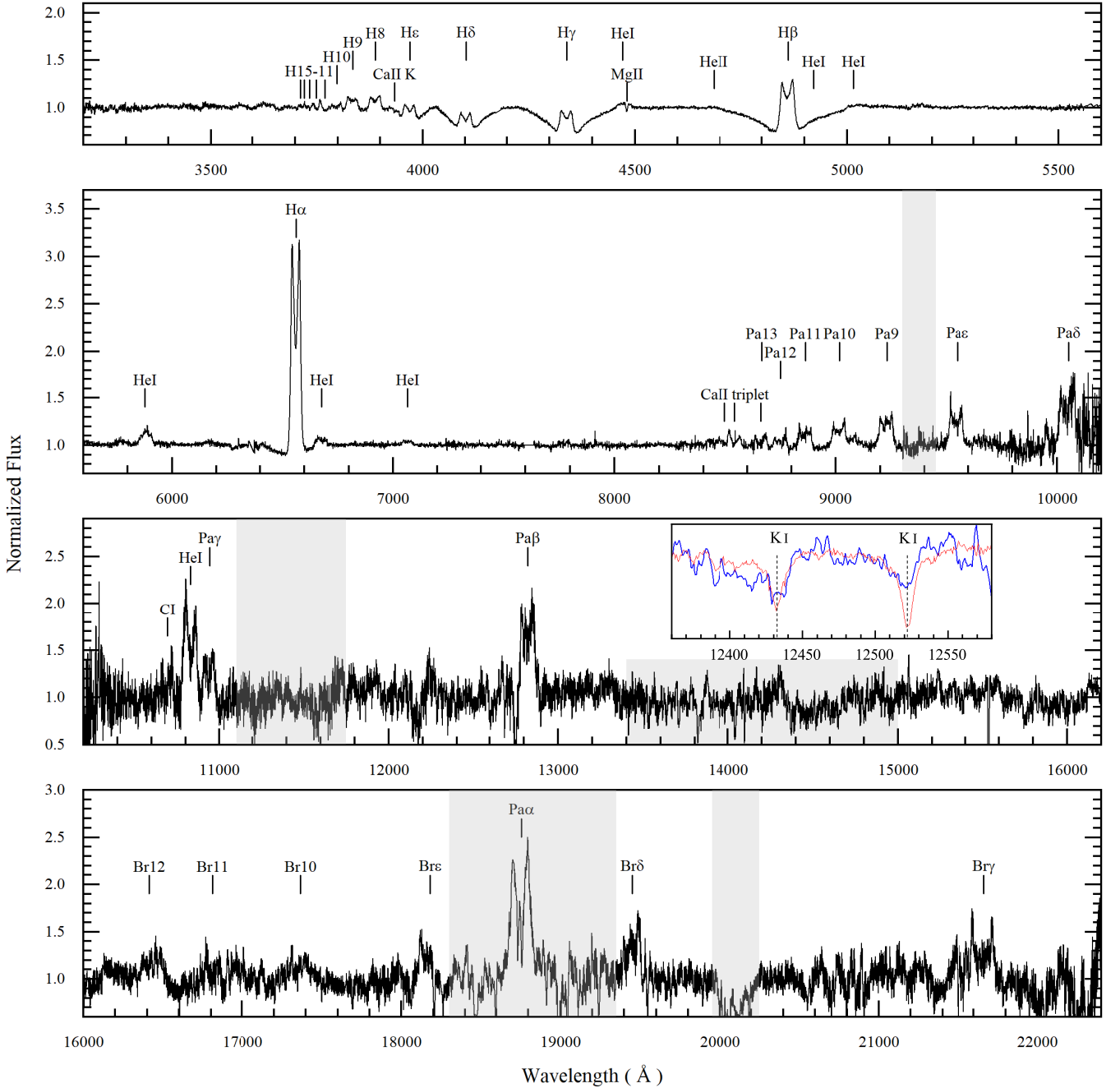


Figure 3. Normalized average spectrum of BW Scl obtained with X-shooter. The most prominent lines are labelled. The regions contaminated by broad telluric absorption bands are highlighted in grey. The inset shows the K I absorption lines, which showed up after the individual spectra of BW Scl were Doppler-corrected into the frame of the donor star (blue line). The red line is the spectrum of the L9 brown dwarf DENIS-P J0255.0–4700.

published times of maxima from [Augusteijn & Wisotzki \(1997\)](#). A linear least-square fit to the O–C values yielded the linear heliocentric ephemeris of the light maxima:

$$T_{\max} = \text{HJD } 245\,0032.18165(26) + 0.0543239136(24) \times E. \quad (1)$$

The new value of the orbital period is very close to that of [Uthas et al.](#)’s ephemeris and results in just a 0.02 phase shift over 25 yr. Below, in Section 5.4, we find the time of the inferior conjunction of the donor star using the X-shooter spectra. This enables us to define an accurate spectroscopic ephemeris, in which phase

zero corresponds to the inferior conjunction of the donor:

$$T_0 = \text{HJD } 245\,0032.13631(11) + 0.0543239136(24) \times E. \quad (2)$$

Thus, the primary light maximum from the ephemeris (1) occurs at spectroscopic phase 0.864 ([Figure 1](#), right).

In addition to the double-humped modulations, [Uthas et al. \(2012\)](#) also reported the detection of a few other photometric variabilities like complex signals with a period near 20 min ($\sim 68 \text{ cycle d}^{-1}$) and a transient ‘quiescent superhump’ signal with a period of $P_{\text{sh}} = 87.27 \text{ min}$. Based on the *TESS* data, we confirm the presence, in the power spectrum, of multiple peaks with periods around 20 min.

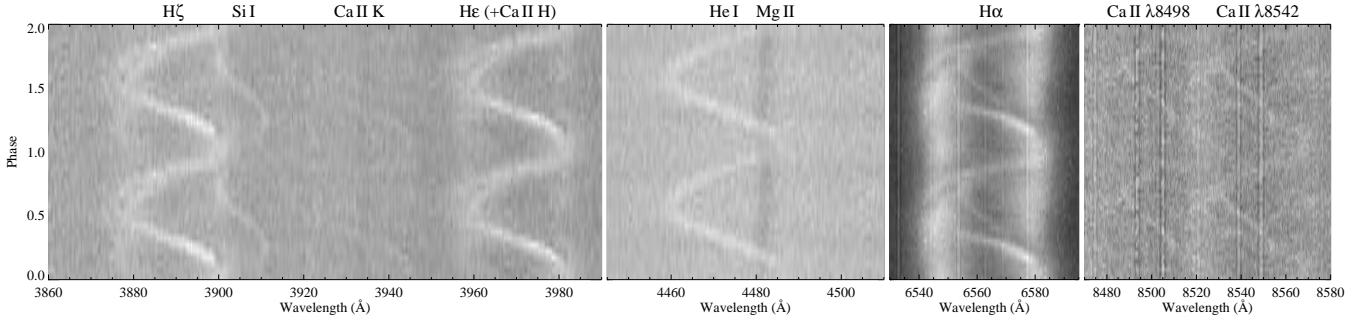


Figure 4. Triled spectra of selected spectral lines from the X-shooter data set, displayed twice for clarity. The shown lines are dominated by one of, or a mixture of emission and absorption components from the irradiated donor star (Si I 3906, Ca II 8498 and 8542, H α), the hotspot (H α , H ϵ , H ζ , He I 4471, Ca II 3934 and 3968), the accretion disc (H α , H ϵ , H ζ , Ca II 8498, 8542), and the WD (Mg II 4481, Ca II 3934). White indicates emission shown in a linear scale.

However, the data obtained before and after the gap show different sets of peaks in this frequency range (see the right inset plot in the left-hand panel of Figure 1). A ‘superhump’ signal is also present (it is much stronger in the ‘after the gap’ data where it reaches a high enough confidence level, see the left inset plot in the left-hand panel of Figure 1) but with a bit different frequency of 16.38 cycle d⁻¹ (~ 87.9 min).

3.2 Long-term photometric evolution

On the long-term time-scale of years the average brightness of BW Scl appears to be quite stable (Figure 2). However, the light curve composed of the photometric observations from the AAVSO, CRTS (Catalina Real-Time Transient Survey; Drake et al. 2009), and ASAS-SN (The All-Sky Automated Survey for Supernovae; Shappee et al. 2014; Jayasinghe et al. 2021) shows that ten years after the superoutburst in 2011, BW Scl has not yet returned to the preoutburst level. Our own photometric measurements indicate that during the EFOSC2 and SOFI observations the object has been ~ 10 percent brighter than during the X-shooter observations.

We also compared the available UV and IR observations obtained between 1999 and 2021 with different telescopes to check for possible variability. We found an excellent agreement between the IR fluxes measured by the *Spitzer Space Telescope* in 2004 (Spitzer Science Center & Infrared Science Archive 2021) and by the *Wide-field Infrared Survey Explorer* in 2010 (the *WISE* mission; Wright et al. 2010) and in 2017–2020 (the *NEOWISE* mission; Mainzer et al. 2011, 2014). All the GALEX measurements obtained in 2003 and 2005 also show no sign of variability with the standard deviation of the data in each band < 0.05 mag, and they are highly consistent with the UVOT observations obtained in 2021 and the *HST* spectroscopy obtained in 1999. Thus, we conclude that during at least 12 yr before the superoutburst (and probably a longer time), BW Scl was at the same flux level.

4 AVERAGED AND TRILED SPECTRA OF BW SCL

Figure 3 shows the normalized average X-shooter spectrum of BW Scl, covering a larger wavelength range and having the highest SNR in the optical domain of all the available data. We note, however, that although all the spectra are similar in appearance, they exhibit a notable difference in the strength of emission lines. In the X-shooter spectrum they are ~ 2 times less intense than in other data sets (Figure A2).

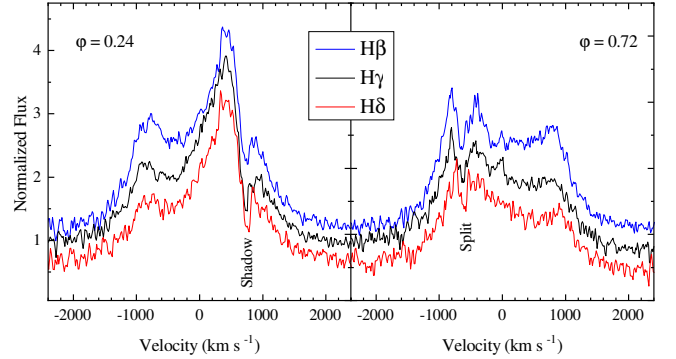


Figure 5. The emission line profiles of H β , H γ , and H δ , obtained with X-shooter at phases 0.24 (left) and 0.72 (right). The profiles show the S-wave shadow and split, correspondingly. The profiles shifted vertically for clarity.

The blue part of the BW Scl spectrum is dominated by broad Balmer absorption lines from the WD with superimposed double-peaked emission components originated in the accretion disc. Balmer emissions can be traced up to H14. Weak emission lines of He I and Ca II 3968 Å are also present. The Mg II 4481 Å absorption line from the WD is clearly visible. At longer wavelengths, besides the H α and He I emission lines, double-peaked hydrogen emission lines of the Paschen and Brackett series are present (can be traced from Pa α up to Pa14 and from Bry up to Br13, respectively). Additionally, we detect the Ca II triplet (8498, 8542, and 8662 Å) and, possibly, a blend of C I lines at ~ 10693 Å, both in emission.

We note that in contrast to the hydrogen *double-peaked* emission lines, all the He I lines except for 10830 Å exhibit, in the averaged spectra, broad smoothed profiles. The reason for it, as shown below, is that the accretion disc appears to be not hot enough to excite helium atoms so as to produce prominent He I lines. Instead, the He I emission comes primarily from the hotspot, the area of interaction between the gas stream and the disc, where the temperature is sufficient.

This and other important details can be found in the phase-resolved triled spectra (Figure 4). It is seen that many lines consist of a mixture of several emission and absorption components originated in the disc, the hotspot, the irradiated donor star, and/or the WD. For instance, all the hydrogen lines (H α , H ϵ , and H ζ are shown in the figure) in addition to the double-peaked emission from the disc also exhibit an S-wave moving in between. This S-wave which originates in the hotspot is the only visible emission component in all

Table 3. Elements of the radial velocity curves of the donor star and the WD derived from the X-shooter spectra.

Spectral lines	K (km s ⁻¹)	γ -velocity (km s ⁻¹)	ϕ_0
Irradiation driven emission lines from the donor:			
Si I 3906	410.0±3.6	-4.8±3.5	0.500±0.002
Fe I 5270+5328+5371	415.9±3.9	-3.4±3.0	0.505±0.002
Ca II triplet	402.6±2.3	-1.9±2.2	0.501±0.002
H α ^a	422.9±7.4	-2.9 (fixed)	0.504±0.004
All lines	405.5±1.4	-2.9±1.4	0.502±0.001
Mg II 4481 from the WD:			
	27.7±3.0	53.0±2.1	-0.003±0.012

^a Fitting of the H α radial velocities was performed using the fixed γ -velocity.

the He I lines except for 10830 Å. Surprisingly, the hotspot S-wave is even visible in the high excitation line of He II 4686 Å, although it is not detected in the Bowen blend. Similar to He II 4686 Å, only the hotspot produces a weak O I 7774 Å emission and there is no sign neither of the disc nor the donor in this line. The Na I doublet around 8190 Å which is a very powerful diagnostic for the donor star in CVs (Friend et al. 1988) is not detected at all.

The Balmer trailed spectra (Figure 4) and even individual Balmer profiles (Figure 5) exhibit interesting features of the S-wave. The S-wave apparently splits between phases 0.5 and 0.9 when it is blue-shifted, and between phases 0.1 and 0.5 a sharp absorption shadow appears which precedes the S-wave. A similar ‘S-wave shadow’ has been reported by Spruit & Rutten (1998) for the prototype object WZ Sge.⁵ We discuss these phenomena in Section 6.3.

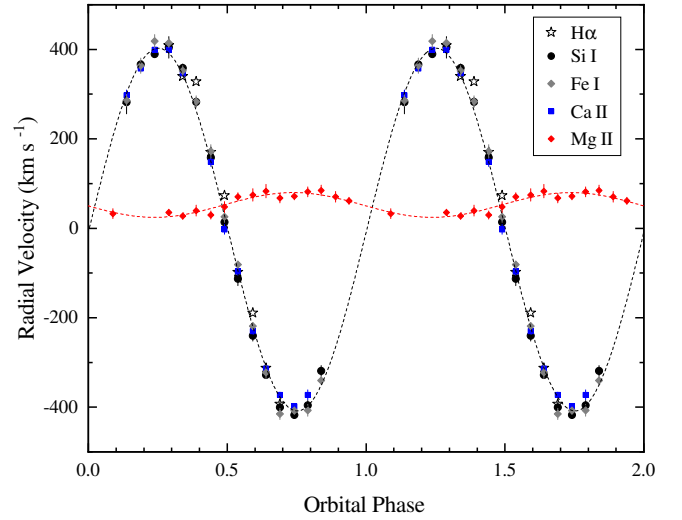
Of special interest is the detection in H α of an additional S-wave with a smaller radial velocity amplitude, which is phase-shifted with respect to the hotspot S-wave. Similar features also detected in a few other lines such as Fe I (5270, 5329, 5372 Å) and the Ca II triplet (8498, 8542, and 8662 Å), but it is most clearly seen in Si I 3906 Å (Figure 4). This sharp emission feature becomes stronger between phases 0.2–0.8 and disappears between phases 0.8–0.2, moving in antiphase with the narrow absorption lines from the WD (in addition to Mg II 4481 Å, such an absorption is also visible in Ca II 3934 Å). All these properties are consistent with being produced by the inner face of the donor companion to the WD. We note that the Si I 3906 Å line is rarely seen in spectra of CVs, but has been detected in some pre-CV objects (see e.g. Parsons et al. 2011).

5 DETERMINATION OF SYSTEM PARAMETERS

5.1 Radial velocities of the donor star

The X-shooter spectra show several irradiation driven emission lines which can be used to measure the radial velocity semi-amplitude of the donor star. Si I 3906 Å is the most clearly visible such a line. It is well detectable in phase-folded spectra manifesting itself as a narrow and sharp peak (Figure 4). The Ca II triplet and Fe I lines are noisier than Si I which makes it difficult to obtain reliable measurements of radial velocities. To suppress noise, we converted the wavelengths to

⁵ Although Spruit & Rutten (1998) did not detect the S-wave splitting, the latter is detectable in the H α and H β trailed spectra of WZ Sge presented by Skidmore et al. (2000), see their fig. 1.

**Figure 6.** Radial velocity fits to the Mg II absorption line from the WD (red diamonds) and emission lines from the donor star (other symbols) in BW Scl.

velocities for each of the line components and combined their fluxes together, separately for Ca II and Fe I. H α is another line in which the irradiation-driven emission component is clearly visible, although it is heavily contaminated by other sources of emission, especially at the phases prior to 0.28. We employed a Gaussian fit to measure the radial velocities of the peaks in Si I and H α and the combined Ca II and Fe I lines. The resulting radial velocity curves were fitted, separately for Si I, Ca II, and Fe I with a sinusoid of the form

$$V(\varphi) = \gamma - K \sin[2\pi(\varphi - \varphi_0)] . \quad (3)$$

We obtained very consistent values for the systemic velocity γ and the phase zero-point ϕ_0 , and slightly different for the radial velocity semi-amplitude $K_2=K$ (Table 3). A limited amount of measurements of H α does not allow constraining the γ -velocity, but by fixing γ at the average value of -2.9 km s⁻¹ we found that the measurements of the H α line and the calculated parameters are very consistent with other lines (see Figure 6 and Table 3).

Although the difference in the K_2 values can be real (these lines originate on the inner hemisphere of the donor star, thus their radial velocities do not track the star’s centre-of-mass), we combined all the measurements together and fitted them again to obtain the final values of $K_2=405.5\pm1.4$ km s⁻¹ and $\gamma = -2.9\pm1.4$ km s⁻¹.

5.2 Rotational and radial velocities of the WD

Narrow absorption lines originated in the photosphere of the WD in BW Scl provide an important tool for measuring radial velocity modulations of the WD and of its rotational velocity. Moreover, these lines are subject to gravitational redshift allowing direct measurement of the WD mass (see e.g. van Spaandonk et al. 2010, and references therein). While the Ca II K absorption line is quite weak and can be detected in the X-shooter spectra only (Figure 4), the Mg II 4481 Å line is strong enough to be visible in both the average UVES and X-shooter data sets. Still, the weakness of the Mg II line coupled together with the low SNR of the UVES spectra prevented us from obtaining realistic measurements of the radial velocities using the UVES data. To measure K_1 , we used the phase-folded X-shooter spectra only, in which radial velocity modulations of Mg II are recognizable even with the naked eye. We note that between the

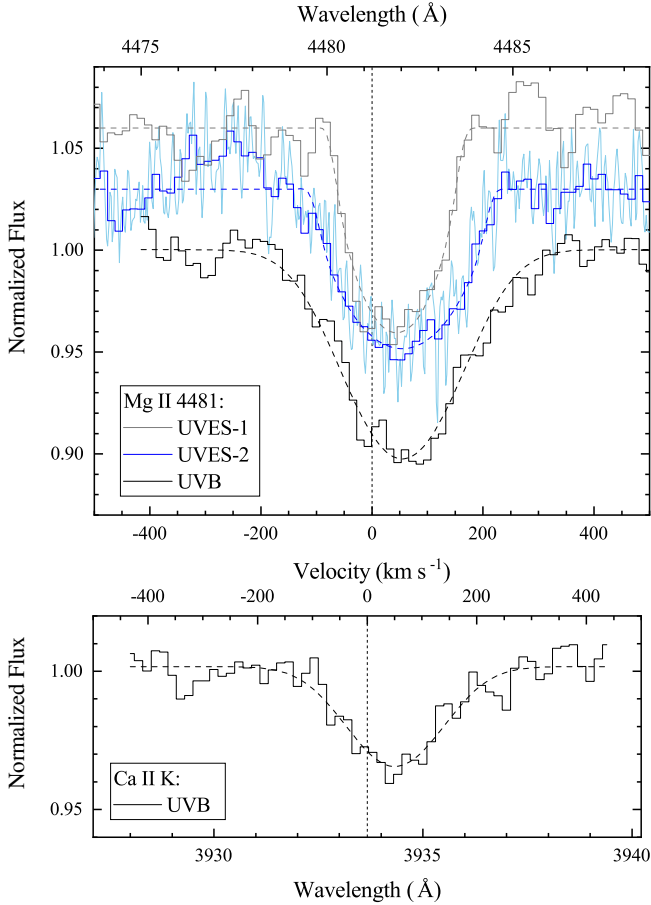


Figure 7. The averaged Mg II line from different data sets normalized to the continuum and shifted upward by 0.03 units (upper panel), and the Ca II K line from the X-shooter spectrum (bottom panel). For display purposes, the noisy UVES spectra were rebinned to the 0.2 Å wavelength step, although the original UVES-2 spectrum is also shown as the light-blue line. The best-fitting rotational broadening profiles are overplotted as dashed lines. The dotted vertical lines indicate the laboratory wavelengths of 4481.21 and 3933.66 Å, respectively.

orbital phases ~ 0.9 and ~ 1.2 the Mg II absorption is contaminated by the He I 4471 Å hotspot emission. For this reason, the corresponded spectra were excluded from the analysis. We followed an interactive approach from Neustroev & Zharikov (2008):

(i) At the first step, we obtained the cross-correlation template spectrum, which was used for measuring the radial velocities of the Mg II 4481 Å line. Initially, the template was obtained by simple averaging of all the UVB spectra.

(ii) Next, the phase-folded spectra were cross-correlated with the template, using the wavelength region 4470–4495 Å. The resulting radial velocity curve was then fitted with the expression (3), and preliminary values of $K_1=K$, the γ velocity, and the phase zero-point ϕ_0 were calculated.

(iii) Each spectrum in the X-shooter data set was then shifted to correct for the orbital motion of the WD, and the results averaged, creating thus a new template.

(iv) Step (ii) was then repeated and the final values of the parameters were calculated which are summarized in Table 3. Figure 6 shows the measured radial velocities together with their sinusoidal fit. Note that the difference between the phase zero-points obtained

from the emission and absorption lines is very close to 0.5, as it must be if the derived velocities from those lines trace the components' motion.

(v) Finally, we repeated step (iii) again, now for all the X-shooter and UVES data sets, using the adopted values of K_1 and ϕ_0 but leaving $\gamma=0$. The obtained average profiles of Mg II (and Ca II K in the X-shooter spectrum) were used to derive the mean radial velocity of the WD and its rotational velocity.

We find that the appearance of the Mg II profile is slightly different in the obtained average spectra (Figure 7, upper panel). The line is less strong in the UVES-2 spectrum, although its FWHM is similar to that of the UVB spectrum. The line in UVES-1 appears more narrow than in the other two spectra. However, this spectrum has a much lower SNR (Table 4) which may affect the line appearance. The Mg II equivalent width (EW) is the largest in the UVB spectrum. This suggests that the Mg II abundance is variable in the WD atmosphere (Holberg et al. 1997).

To derive the mean radial velocity of the WD, v_{rad} , and its rotational velocity, $V_{\text{rot}} \sin i$, we fitted the Doppler-corrected co-added Mg II and Ca II K profiles with a synthetic profile which was smoothed to the corresponded spectral resolution of the data set and rotationally broadened using the PYASTRONOMY⁶ function ROTBROAD (Czesla et al. 2019). Because the Mg II 4481 Å line is a triplet with the components at 4481.126, 4481.150, and 4481.325 Å whose transition probabilities are $\log(gf) = 0.7367$, -0.5643 , and 0.5818 , respectively, for the fitting we used a spectral model based on a list of Gaussian lines from PYASTRONOMY's MODEL SUITE (PYASTRONOMY.MODELSUITE.LLGAUSS). The rotational broadening solution depends upon the limb-darkening which, to the best of our knowledge, has never been evaluated for metal spectral lines from WDs. However, the limb-darkening coefficients have been computed for a number of broad-band photometric filters (see e.g. Claret et al. 2020). For the range of expected parameters of the DA WD in BW Scl ($T_{\text{eff}} \sim 12000\text{--}15000$ K, $\log g \sim 8.25\text{--}8.75$), the linear limb-darkening coefficient ε (PYASTRONOMY uses a linear approximation) in the B -band varies between ~ 0.32 and 0.38 . We assumed $\varepsilon = 0.35$ in deriving the rotational broadening. All fits yield fairly consistent results but with slightly different values of the rotational velocity from the Ca II and UVES-1 Mg II profiles (Table 4). As it has been shown by van Spaandonk et al. (2010), the low SNR of the spectrum and the line weakness can affect the determination of the model parameters. Using the SNR as a weighting factor, we calculated the averaged values of $v_{\text{rad}} = 54.6 \pm 3.0$ km s⁻¹ and $V_{\text{rot}} \sin i = 139 \pm 6$ km s⁻¹. The found rotational velocity of the WD in BW Scl is consistent with Gänsicke et al. (2005), but it appears relatively slow in comparison with other accreting WDs (Sion & Godon 2022).

5.3 The mass of the WD from the gravitational redshift

The observed Mg II and Ca II velocity $v_{\text{obs}} = v_{\text{rad}} = 54.6 \pm 3.0$ km s⁻¹ is a sum of the systemic velocity γ and the gravitational redshift v_{grav} :

$$v_{\text{obs}} = \gamma + v_{\text{grav}}. \quad (4)$$

γ is most accurately measured from radial velocity variations of the donor star (the contribution of the low-mass secondary to the redshift is negligible). Adopting the Si I + Ca II + Fe I value $\gamma = -2.9 \pm 1.4$

⁶ <https://github.com/sczesla/PyAstronomy>

Table 4. Measurements of the Mg II 4481 Å and Ca II K lines.

Data set	SNR	EW (Å)	FWHM (Å)	Line strength	v_{rad} (km s ⁻¹)	$V_{\text{rot}} \sin i$ (km s ⁻¹)
UVES-1	30	0.30	2.9	0.90	44.3±4.2	117±5
UVES-2	105	0.27	3.6	0.92	53.8±3.4	151±5
UVB (Mg II)	165	0.38	3.6	0.90	55.2±2.3	140±6
UVB (Ca II)	140	0.07	2.0	0.96	55.6±4.5	101±15
average					54.6±3.0	139±6

km s⁻¹ from Table 3, we obtain $v_{\text{grav}} = 57.5 \pm 3.3$ km s⁻¹. The gravitational redshift depends on the ratio between mass and radius (Greenstein & Trimble 1967):

$$v_{\text{grav}} = \frac{GM}{cR} = 0.637 \frac{M_{\text{WD}}}{M_{\odot}} \frac{R_{\odot}}{R_{\text{WD}}} \text{ km s}^{-1}, \quad (5)$$

where G is the gravitational constant, c is the speed of light, and R_{WD} and M_{WD} are the radius and the mass of the WD, respectively. Using Nauenberg's analytic mass–radius relation for WDs (Nauenberg 1972; Cook & Warner 1984), we get $M_{\text{WD}} = 0.87 \pm 0.03 M_{\odot}$. However, this value needs to be lowered since Nauenberg's relation assumes a cold, non-rotating WD, providing thus only a lower limit to the WD radius for a given mass. The radius of a WD at a given temperature and mass depends on the thickness of the hydrogen layer at the WD surface (Romero et al. 2019). According to Bédard et al. (2020), a WD with the mass of 0.8–1.0 M_{\odot} and the temperature of ~15000 K has the radius about 2 per cent larger than that of a cold WD in case of a thin hydrogen layer, and about 3 per cent in case of a thick layer. Because the thickness of the hydrogen layer is not known, in the following we adopt the average conservative value $M_{\text{WD}} = 0.85 \pm 0.04 M_{\odot}$, which corresponds to the surface gravity of $\log g = 8.40 \pm 0.02$. The found mass of the WD in BW Scl is consistent with the mean WD mass in CVs of $0.81^{+0.16}_{-0.20} M_{\odot}$ (Pala et al. 2022; Zorotovic et al. 2011) but appears less than that deduced by Pala et al. (2022) from the UV spectral fit ($1.007 \pm 0.012 M_{\odot}$).

5.4 System parameters

The detection of radial velocity variations of both stellar components and a direct measurement of the WD mass via gravitational redshift enable us to fully determine the orbital and stellar parameters of the binary. The ratio of the radial velocity semi-amplitudes of the primary and secondary stars K_1 and K_2 gives the mass ratio q

$$q = \frac{M_2}{M_1} = \frac{K_1}{K_2}. \quad (6)$$

Combining the values of K_1 , K_2 , P_{orb} , and $M_1 = M_{\text{WD}}$ we can find the system inclination i , the mass of the donor M_2 , and the binary separation a :

$$M_1 \sin^3 i = \frac{PK_2(K_1 + K_2)^2}{2\pi G}, \quad (7)$$

$$M_2 \sin^3 i = \frac{PK_1(K_1 + K_2)^2}{2\pi G}, \quad (8)$$

$$a \sin i = \frac{P(K_1 + K_2)}{2\pi}. \quad (9)$$

Here we have to note that the *observed* value of $K_2 = K_{2,o}$ represents

Table 5. Orbital and system parameters for BW Scl.

Parameter	Value based on the corrected $K_2 = K_{2,\text{true}}$
P_{orb} (d)	0.0543239136(24)
T_0 (HJD)	245 0032.13631(11)
K_1 (km s ⁻¹)	27.7±3.0
$K_{2,o}$ (km s ⁻¹)	405.5±1.4
$K_{2,\text{true}}$ (km s ⁻¹)	461±13
γ (km s ⁻¹)	-2.9±1.4
$q = M_2/M_1$	0.060±0.006
M_{wd}/M_{\odot}	0.85±0.04
M_2/M_{\odot}	0.051±0.006
i	64.3°±3.6°
a/R_{\odot}	0.58±0.02
R_2/R_{\odot} (volume radius)	0.103±0.005
$r_{\text{d,max}}/R_{\odot}$	0.338±0.001

only a lower limit to the true radial velocity semi-amplitude $K_{2,\text{true}}$ because the detected emission lines are irradiation-induced from the surface of the donor star facing the WD. The non-coincidence of the centre-of-mass and the centre-of-light of the donor results in systematic errors in the determined $K_{2,o}$. Therefore, in order to obtain the true value of K_2 , a K -'correction' should be applied (Wade & Horne 1988). The K -correction can be expressed as:

$$\frac{K_{2,o}}{K_2} \approx 1 - 0.462q^{1/3}(1+q)^{2/3}f, \quad (10)$$

(equation 2.77 in Warner 1995), where $f = \Delta R_2/R_2$ is the ratio of the displacement of the centre-of-light from the centre of mass of the secondary star to the radius of the secondary. For $f=0$ the emission is spread uniformly across the entire surface of the donor, $f=0.5$ roughly corresponds to the extreme case where the spectral line comes only from the hemisphere closest to the WD, and for $f=1$ all the emission comes from the donor surface near the inner Lagrangian point. It is difficult to quantify the f -factor, but it seems to depend on the optical depths of spectral lines that can explain the scatter of the measured values of $K_{2,o}$ for different lines (see also our Table 3). According to Parsons et al. (2010, 2012), $f \approx 0.77$ for an optically thin line, and $f=0.5$ for optically thick emission. Using these values, we obtain $K_{2,o}/K_{2,\text{true}} = 0.88 \pm 0.02$ and, accordingly, $K_{2,\text{true}} = 461 \pm 12$, where 0.02 and 12 are not the standard deviations but rather adopted ranges of values.

Now, from the above equations, we find $q = 0.060 \pm 0.007$, $M_2 = 0.051 \pm 0.006 M_{\odot}$, $i = 64.3 \pm 3.6^\circ$, and $a = 0.584 \pm 0.020 R_{\odot}$. These and other deduced system parameters are listed in Table 5. The table also shows the tidal truncation radius of the disc $r_{\text{d,max}}$, calculated using updated approximation formula (3) from Neustroev & Zharikov (2020). $r_{\text{d,max}} = 0.338 R_{\odot} = 0.58 a$ corresponds to the minimal possible Keplerian velocity in the disc of $v_{\text{out}} = 693$ km s⁻¹, and the minimal observed velocity $v_{\text{min}} = v_{\text{out}} \sin i = 624$ km s⁻¹.

6 THE WD, DONOR STAR, AND ACCRETION DISC

6.1 Temperature of the WD in BW Scl

The blue spectrum of BW Scl is dominated by the characteristic broad Balmer absorption lines from the DA WD, which can be used to evaluate the WD effective temperature T_{eff} and surface gravity $\log g$. These parameters of isolated WDs are often estimated through

a spectral fit of a grid of WD synthetic atmosphere models to the observed absorption lines. In accreting WDs, the WD spectrum is contaminated by the accretion disc and the donor star, which makes it a more complex task to determine T_{eff} and $\log g$. While the disc lines can be cut out of the spectrum, the shape of the disc continuum is still unknown. The latter is often assumed to follow a simple power law, although it has been shown that in the low mass transfer rate regime the disc emission appears to be better reproduced by a hydrogen slab model (see, e.g., [Hernández Santisteban et al. 2016](#); [Pala et al. 2018, 2019, 2022](#)). Nevertheless, given that the hydrogen slab is a multiparameter model and that we include in our analysis only a relatively short portion of the spectrum, in the following we use a power law as a first approximation to the disc continuum.

Our fitting procedure can be described as follows. We use the flux calibrated average spectra, in which we consider only the H β , H γ and H δ lines because the width of higher-order Balmer lines of the WD in BW Scl becomes comparable with that of the disc emission component. We cut out the emission cores of these lines and then perform the χ^2 fit of the object spectrum to a grid of synthetic spectra of DA WDs, to which the power-law flux was added. We used a grid of [Koester \(2010\)](#) model atmospheres⁷ that cover a broad range of T_{eff} in steps of 250 K and $\log g$ in steps of 0.25. Using linear interpolation from the grid, we also produced additional model spectra for $\log g$ in step of 0.05. The model spectra were convolved with the appropriate Gaussian instrumental profile to match the spectral resolution of observed spectra. From an extensive testing of this technique ([Hedemäki 2021](#); Neustroev & Hedemäki, in preparation⁸), it has been shown that even for a large contribution of a power-law component ($\geq 100\%$), a low SNR ~ 30 , and relatively broad emission cores eliminated from the fitting procedure (up to $\pm 4000 \text{ km s}^{-1}$), uncertainty estimates of parameters were within our grid steps ($\Delta T_{\text{eff}} = 250 \text{ K}$ and $\Delta \log g = 0.25$).⁹

The knowledge of the distance d to the source helps to significantly increase the reliability of parameter estimates, allowing the WD flux to be scaled correctly. The relation between observed fluxes F_{obs} and model Eddington fluxes H is

$$F_{\text{obs}} = 4\pi H \frac{R_{\text{WD}}^2}{d^2}, \quad (11)$$

where R_{WD} and d are in the same units. In our fitting procedure, we link $\log g$ and R_{WD} using an approximation formula which is based on Nauenberg’s mass–radius relation:

$$R_{\text{WD}}/R_{\odot} = (0.4074 - 0.0368 * \log g)^2. \quad (12)$$

It is accurate to better than 1% over the range $6.5 < \log g < 9.35$ ($0.1 M_{\odot} < M_{\text{WD}} < 1.35 M_{\odot}$).

The surface gravity of the WD in BW Scl is already known from the gravitational redshift, thus simplifying our problem even further. This allowed us to fix $\log g$ at 8.40 and apply the described technique to each average spectrum of BW Scl, resulting in $T_{\text{eff}} = 14250 \text{ K}$ for

the X-shooter and NTT spectra¹⁰ and 13250 K for both the UVES spectra ([Table 6](#)). We note that the values of T_{eff} as derived from the UVES observations are 1000 K lower than that from the X-shooter spectrum. Given that the UV and optical fluxes of BW Scl were very stable for many years before the superoutburst (see [Section 3.2](#)), we assume (although cannot be sure) that this difference may not be real and that the UVES T_{eff} ’s are underestimated due to low quality of those spectra. For this reason, we fixed T_{eff} at 14250 K and repeated the fitting procedure for the UVES data. The WD temperature found from the best quality data (X-shooter and NTT) is lower than that derived by [Pala et al. \(2022\)](#). One of the reasons for that might be a smaller radius (due to a higher mass) of the WD in their solution.

6.2 Spectral energy distribution and accretion disc spectra

Combining our multiwavelength data with the archival UV and NIR observations, we reconstructed the spectral energy distribution (SED) of BW Scl in the UV-optical-NIR wavelengths at the time of the X-shooter ([Figure 8](#)) and NTT observations. As seen in [Figure 8](#) and [Table 6](#), the UV-optical-NIR spectrum is dominated by the WD component which produces around 80–90 per cent of the flux in the blue wavelength range. However, a non-WD contribution increases with longer wavelengths and becomes dominant at about 13000 Å. The SED appears very smooth. No sign of the donor star is visible, but one can notice a hint of a “knee” at $\sim 30000\text{--}40000 \text{ Å}$. Here we have to note that although in short-period CVs with a main-sequence donor star the NIR hump in the SED should not be expected to be as pronounced as in longer period CVs with a low mass-transfer rate (as seen, e.g., in RZ Leo – [Neustroev et al. 2017](#)), it can still be detectable (see figure 1 in [Neustroev et al. 2018a](#)). On the other hand, a sub-stellar donor in a period bouncer is expected to be so dim that the WD and even relatively weak accretion disc can outshine it.

In order to put an upper limit on the donor contribution to the total system light, we subtracted the underlying WD spectrum from the observed SEDs. This allowed recovering not only a non-WD continuum but also higher-order Balmer emission lines which were sitting inside the WD absorption troughs. In the following, we call the resulting spectra as the spectra of the accretion disc. We admit that they are contaminated by the donor star, but we show below that the contribution of the donor is very low.

[Figure 9](#) shows the disc spectra recovered from the X-shooter and NTT data sets. The Balmer and Paschen continuum flux was larger during the post-outburst NTT observations. The spectra display a strong Balmer jump and a notable Paschen jump, both in emission. Overall, the spectra strongly resemble those produced in a hydrogen gas slab (compare with, e.g. fig. 12 in [Pala et al. 2018](#)). While the disc spectra will be analysed in detail elsewhere, here in [Tables 6](#) and [7](#) we outline different parameters of the continuum light and of the most prominent Balmer lines that were measured from the accretion disc spectra. In particular, the spectra were convolved with the standard Johnson and Kron–Cousins *UBVR_IcJHK* filter band-passes, and the broad-band absolute magnitudes were determined. Note that although the magnitudes vary slightly from spectrum to spectrum, M_V appears consistent with an indirect estimate presented by [Patterson \(2011, table 3\)](#).

We can now compare the observed disc spectra with the SEDs of stars of different temperatures. For this, we used tables 2, 5, and 6 from [Knigge et al. \(2011\)](#) which provide the absolute magnitudes

¹⁰ We point out that when $\log g$ is allowed to vary, the best solution is also found at $\log g = 8.40$, exactly consistent with the gravitational redshift.

⁷ [Koester \(2010\)](#) synthetic spectra of DA WDs were retrieved from <http://svo2.cab.inta-csic.es/theory/newov2/index.php?models=koester2>

⁸ <https://vitaly.neustroev.net/research/wd-parameters/>

⁹ Obviously, these errors represent only the ability of the model spectra to match the observed spectra and most likely are underestimated. An example of more accurate analysis of the errors associated with measurements of WD parameters can be found in [Kepler et al. \(2007\)](#). In particular, using Monte Carlo simulations, they estimated an uncertainty of around $\Delta T_{\text{eff}} \approx 500 \text{ K}$ and $\Delta \log g \approx 0.10$ at SNR = 40 for the whole spectra fitting.

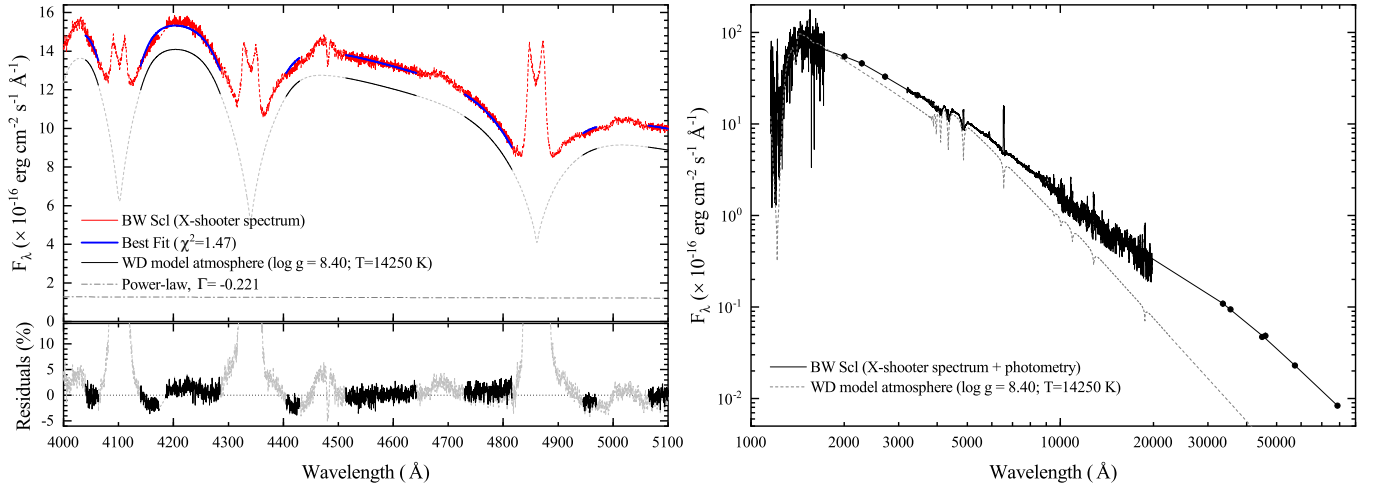


Figure 8. Left: the X-Shooter spectrum (red) along with the best-fitting model (blue). The WD emission (black) and a power-law component (grey dash-dotted line) contribute 90 and 10 per cent of the total flux at 4600 Å, respectively. The masked spectral areas are plotted by dashed lines. Right: the SED of BW Scl, shown together with the best-fitting WD model spectrum.

Table 6. The WD temperatures and the disc contribution to the total flux at 4600 Å. Also shown the parameters of the Balmer emission lines in the disc spectra.

Data set	T_{eff} (K) (log $g=8.4$)	F_d/F_{total} (%)	Equivalent width (Å)				Flux ($\times 10^{-14}$ erg cm $^{-2}$ s $^{-1}$)				Balmer decrement H α : H β : H γ : H δ
			H α	H β	H γ	H δ	H α	H β	H γ	H δ	
UVES-1	13250	17	360	201	180	125	6.3	4.3	3.8	3.3	1.46 : 1.00 : 0.89 : 0.75
	14250 (fixed)	5	450	415	545	385	6.3	4.6	4.2	3.6	1.35 : 1.00 : 0.90 : 0.79
UVES-2	13250	19	—	225	135	120	—	4.8	3.5	3.4	: 1.00 : 0.74 : 0.70
	14250 (fixed)	5	—	450	370	400	—	4.9	3.8	3.7	: 1.00 : 0.78 : 0.75
X-shooter	14250	10	341	210	190	170	4.8	2.8	2.4	2.0	1.71 : 1.00 : 0.86 : 0.71
NTT	14250	19	340	194	178	174	7.2	4.5	4.0	3.7	1.60 : 1.00 : 0.89 : 0.82

Table 7. The broad-band absolute magnitudes of the accretion disc derived from different data sets. Also shown the predicted absolute magnitudes of brown dwarfs with $T_{\text{eff}}=1618$ and 1945 K and the radius $0.103 R_{\odot}$ (Knigge et al. 2011).

Data set	M_U	M_B	M_V	M_R	M_I	M_J	M_H	M_K
Accretion disc:								
UVES-1 ($T_{\text{WD}}=13250$ K)	12.17	13.21	13.19					
UVES-1 ($T_{\text{WD}}=14250$ K)	12.55	13.69	13.63					
X-shooter	12.35	13.76	13.66	12.96	12.64	12.01	11.41	10.78
NTT	11.85	13.11	12.99	12.51	12.29	11.74	11.27	10.65
Brown dwarf ($T_{\text{eff}}=1618$ K)								
Brown dwarf ($T_{\text{eff}}=1945$ K)	30.66	25.46	22.97	18.98	16.13	12.76	12.60	12.54
	28.86	24.57	21.38	18.32	15.90	12.39	11.65	11.17

of the donor along the CV evolution sequence. We extracted the magnitudes of a few stars with T_{eff} between 1320 and 2254 K, and converted them into fluxes, scaling to the distance of BW Scl and the radius of its donor ($0.103 R_{\odot}$). We also used observed brown dwarf spectra, which were scaled to be in accordance with the above-predicted fluxes. These spectra exhibit a characteristic series of broad peaks near 1.08, 1.27, 1.65, and 2.08 μm . Taking into account the noise level in the NIR spectra, we put a conservative upper limit on the donor temperature to be $T_{\text{eff},2} \lesssim 1600$ K, otherwise the mentioned flux peaks will become obvious *even assuming* that the disc spectrum declines strongly toward longer wavelength in the NIR. However, the donor temperature should not be much lower than that because we see a sign of the donor K I absorption lines (12432

and 12522 Å) in the averaged spectrum corrected for orbital motion of the donor star (see the inset panel in Figure 3). The spectra and calculated SEDs of two brown dwarfs with $T_{\text{eff}}=1618$ and 1948 K are shown in Figure 9 together with the disc spectra. We find it instructive to include their magnitudes into Table 7, allowing for a direct comparison between the donor and observed fluxes.

By integrating the disc SEDs over all wavelengths, we can put a conservative upper limit on the bolometric luminosity of the accretion disc and on the mass-accretion rate. The latter can be calculated using

$$\dot{M}_{\text{acc}} = \frac{2L_d R_{\text{wd}}}{GM_{\text{wd}}}. \quad (13)$$

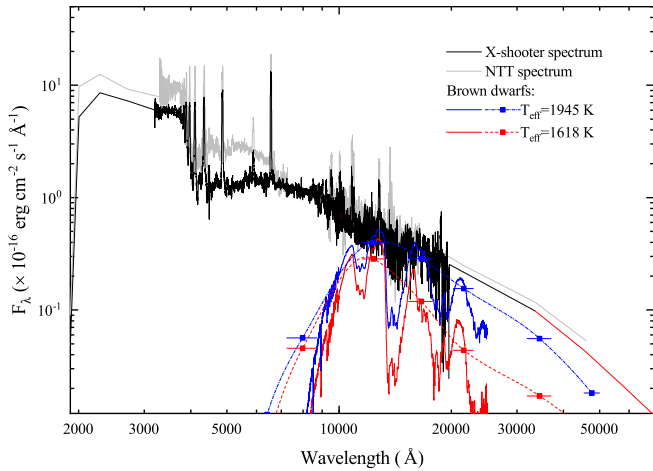


Figure 9. The accretion disc spectra, shown together with the theoretical SEDs and observed spectra of two brown dwarfs (see the text for details).

We find these parameters for the X-shooter spectrum to be $L_d \lesssim 3.2 \times 10^{30} \text{ erg s}^{-1}$ and $\dot{M}_{\text{acc}} \lesssim 3.7 \times 10^{13} \text{ g s}^{-1} = 5.9 \times 10^{-13} M_{\odot} \text{ yr}^{-1}$, and $L_d \lesssim 4.0 \times 10^{30} \text{ erg s}^{-1}$ and $\dot{M}_{\text{acc}} \lesssim 4.6 \times 10^{13} \text{ g s}^{-1} = 7.4 \times 10^{-13} M_{\odot} \text{ yr}^{-1}$ for the NTT spectrum. These estimates include the contribution from the donor which is less than 8 per cent. We also point out that the disc luminosity L_d appears to be a few times larger than the X-ray luminosity (see Section 2.2). This is consistent with the observations of other short-period CVs (Neustroev et al. 2018b; Amantayeva et al. 2021), and with the disc instability model according to which the mass-accretion rate in the quiescent disc is expected to decrease steeply with decreasing radius (Cannizzo 1993; Ludwig et al. 1994). The latter means that accretion rates at the WD surface should be smaller than in the outer disc. Thus, the X-ray flux which almost certainly originates in regions very close to the WD surface should indeed be quite low.

6.3 Doppler tomography

The trailed spectra of BW Scl exhibit a mixture of different variable emission components. In order to study the sources of emission in more detail, we used Doppler tomography (Marsh & Horne 1988; Marsh 2001). We produced a large number of tomograms, using the code developed by Spruit (1998). Bearing in mind the unprecedented quality of the X-shooter data, in this section we show the most representative lines from this data set only. Figures 10, 11, and 12 display the Doppler maps of H α , H γ , and He I 5876 together with the trailed spectra and their corresponding reconstructed counterparts. However, supplementary Figures A3, A4, and A5 provide a comparison of Doppler maps of H α and H β from different data sets. They look very consistent to each other, indicating no notable difference in the disc structure at different epochs. Also, as seen from Figure 12, the helium lines represent a simple case in terms of their orbital variability, so in Figure 13 we only show the maps of the He lines, omitting unnecessary trailed spectra.

We start the discussion of Doppler tomography with the H α line as it is the strongest line in the spectra (see the upper row of Figure 10, and also Figure A3). The maps are dominated by a ring of disc emission and a compact, relatively weak hotspot emission which is located in the fourth quadrant ($-V_x, +V_y$) of the maps. We note that all Balmer lines display a gap in the upper part of the disc ring. In addition to different marks on all the maps that facilitate interpreting the tomograms (see the captions to Figure 10), for H α we also show

the circles representing velocities at the tidal truncation radius r_{max} , u_{min} , and at the 3:1 resonance radius $r_{3:1}$, assuming a circular Keplerian flow in the disc. It is seen that the emission extends beyond $r_{3:1}$ and is close to the truncated orbit. This is in accordance with other studies reporting that the accretion disc in CVs is always extended to its truncation limit (Neustroev et al. 2016; Neustroev & Zharikov 2020; Amantayeva et al. 2021).

The hotspot emits at a very wide range of velocities. It occupies a larger than $500 \times 400 \text{ km s}^{-1}$ area on the Doppler maps, reflecting a large width of the hotspot S-wave. The latter can be compared with e.g. the donor S-wave in H α , or the NaD night-sky lines, which are seen in the trailed spectrum of He I 5876 in Figure 12. The location of the hotspot area on the maps is basically consistent with the trajectory of the gas stream, showing a mixture of the ballistic and Keplerian velocities along the stream. Although the hotspot has a complex, arrow-like structure, the peak of spot emission agrees better with the ballistic stream trajectory and locates well inside the disc, as close to the WD as $r_{\text{hs}} \approx 0.35\text{--}0.40 a \approx 0.6\text{--}0.7 r_d$.

The H α tomogram shows only a weak sign of the donor star. Comparing the observed trailed spectrum with its reconstructed counterpart (the central and right plots in the upper row of Figure 10), one can notice that the latter is also missing the sharp emission component produced by the donor. The reason for it is that this weak feature is visible only during half of the orbital period and disappears during another half. This violates an assumption of Doppler tomography that all points are equally visible at all times (Marsh 2001). In order to overcome this problem, we calculated another tomogram using only about 60 per cent of spectra between phases 0.2–0.8. Now the donor is obvious in both the map and the corresponded reconstructed trailed spectrum (the lower row of Figure 10). By using the same approach, we also calculated the maps of other lines (Si I, Fe I, and Ca II) in which we detected the donor star. Zoomed parts of these maps that are centred around the donor area are shown in Figure 14.

It is interesting that the hotspot looks differently on the *donor-on* map of H α compared with the tomogram, calculated using the whole phase range of spectra. This may indicate that the radiation emitted by the hotspot is anisotropic. To study the hotspot area and the presence of anisotropy in more detail, we used higher order Balmer lines in which the hotspot reaches a higher contrast with respect to the disc than in H α (see the maps and trailed spectra of H γ and H β in Figures 11 and A5, respectively). We point out that, similar to the case of the donor emission, the trailed spectra reconstructed from the maps of the whole phase range are missing some distinctive features of the S-wave which are clearly visible in the observed trailed spectra. The most prominent of them are the S-wave splitting and shadow, marked on the observed trailed spectrum in Figure 11 (see also Figure 5). It is likely that these two features are related to each other as the shadow is seemingly transitioning into one of the split S-waves at phase ~ 0.5 , or is creating this apparent split (see the trailed spectra in Figures 11 and A5). Another interesting feature has first been mentioned by Spruit & Rutten (1998) in their study of WZ Sge. They detected the disappearance of the S-wave around phase 0.6, which we also confirm for the bluer, higher velocity S-wave of BW Scl. Some of these features in WZ Sge were interpreted by Spruit & Rutten (1998) in terms of finite optical-depth effects.

Whatever is the reason for such a behaviour of the S-wave, its source violates another assumption of Doppler tomography: it changes visibility or projected size, resulting in a changed flux. To ease this problem, we applied the approach used above to recover the donor emission. We calculated 2 Doppler maps for each of H β and H γ , using again 60 per cent of spectra centred on phases 0.25 (0.95–0.55) and 0.65 (0.35–0.95). The new reconstructed trailed spectra

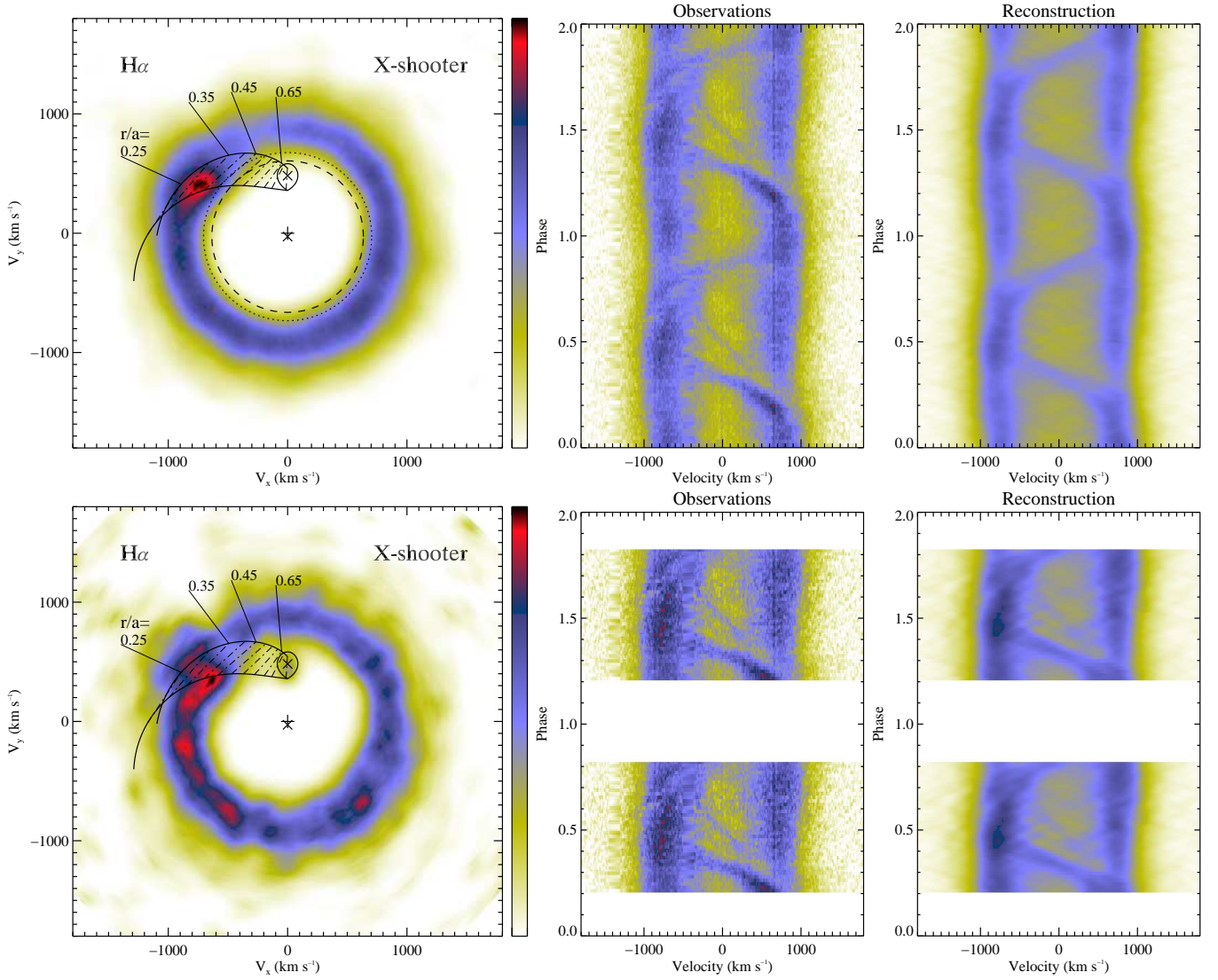


Figure 10. The Doppler maps and corresponding observed and reconstructed trailed spectra of the H α emission line. The upper map is calculated using the whole set of spectra, whereas for the lower map only 60 per cent of spectra between phases 0.2–0.8 were used. Marked on the maps are the position of the WD (lower cross), the centre of mass of the binary (middle cross) and the Roche lobe of the donor star (upper bubble with the cross). The dashed and dotted circles show the tidal truncation radius r_{max} and the 3:1 resonance radius $r_{3:1}$, respectively. The dashed lines connect the velocity of the ballistic gas stream (lower curve) and the velocity on the Keplerian disc along the gas stream (upper curve) for the same points at distances labelled along the upper curve (in r/a units). These lines are separated by $0.05r/a$.

reproduce the observed ones in great detail. Both the S-wave splitting, the shadow, and even the disappearance of the S-wave at phase 0.6 are clearly visible now. Amazingly, the visual appearance of the hotspot area on the new maps has changed dramatically. The hotspot looks absolutely different when watching from different directions, confirming the strong anisotropy of the emission.

The spectra centred on phase 0.25 produce on the Doppler map a long and relatively narrow stream of emission starting at $r \approx 0.6a$ from the WD, at the disc edge, and basically following the ballistic trajectory until $r \approx 0.25a$. Above this emission region, there is a horizontally extended area with no emission from the disc. It is this feature that causes the S-wave shadow. In the following, we call it as ‘an empty spot’. Its position on the map ($V_x \approx -400$, $V_y \approx +800$) roughly coincides with the gap in the disc, which we mentioned above.

Both these features appear inverted on the second map which is based on the spectra centered on phase 0.65. The former stream of

emission has now a brightness of the underlying disc, but on both sides of it, above and below on the map, it is accompanying by two newly appeared emission streams. The lower stream roughly follows the ballistic trajectory, but located slightly below it on the map. The upper emission stream follows Keplerian velocities along the trajectory of the gas stream, although also located above it. The position of the latter emission feature on the map roughly coincides with the empty spot.

Comparing these two maps, we can also notice a different contrast of the hotspot with respect to the underlying disc. The maps are scaled according to their minimum and maximum values. The weaker appearance of the disc on the maps centred on phase 0.25 means that from this direction the hotspot appears brighter and more compact than from the perpendicular direction.

A sharp contrast between the two maps motivated us to calculate a sort of a dynamical Doppler map of H γ which allow examining the

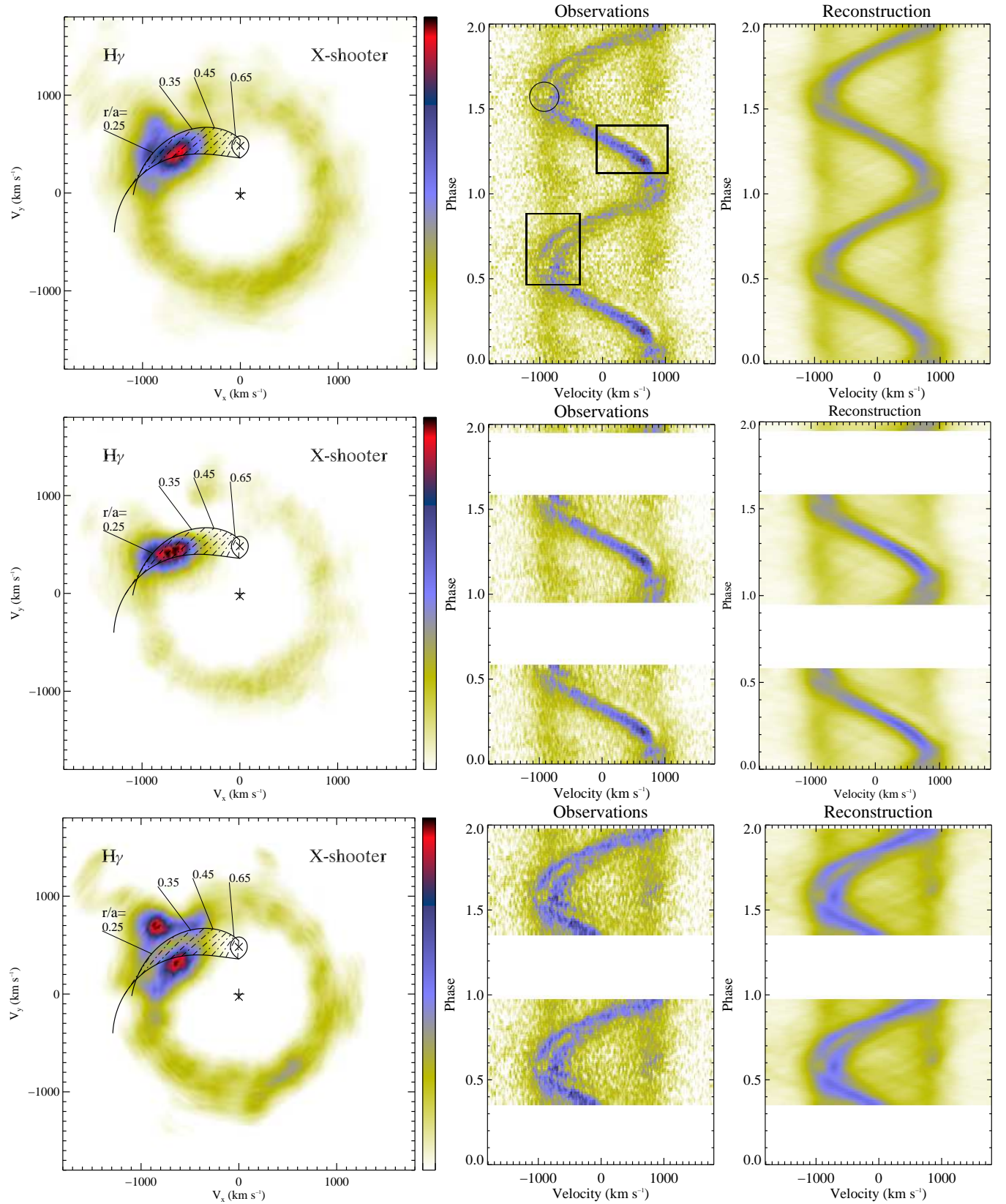


Figure 11. Same as Figure 10, for H γ . Marked on the observed trailed spectrum are the positions of the S-wave split and the S-wave shadow (the left and right rectangles, respectively), and the S-wave disappearance around phase 0.6 (circle). The middle and lower maps were calculated using 60 per cent of spectra centred on phases 0.25 and 0.65, respectively.

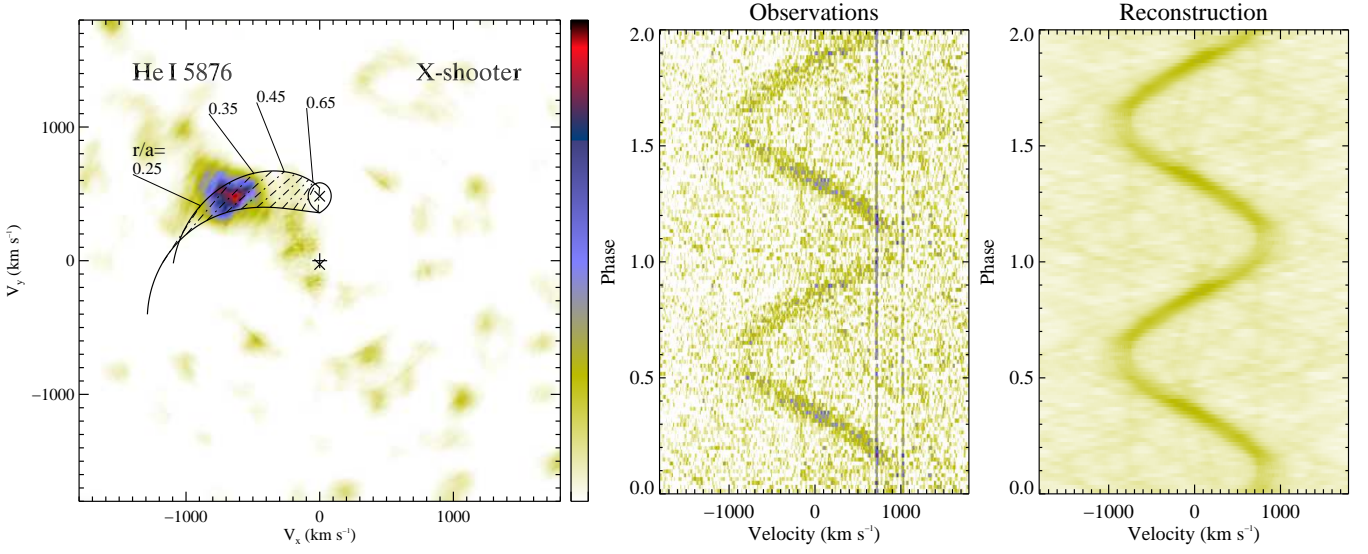


Figure 12. Same as Figure 10, for He I 5876 Å. In the observed trailed spectrum, the Na D night-sky lines are seen.

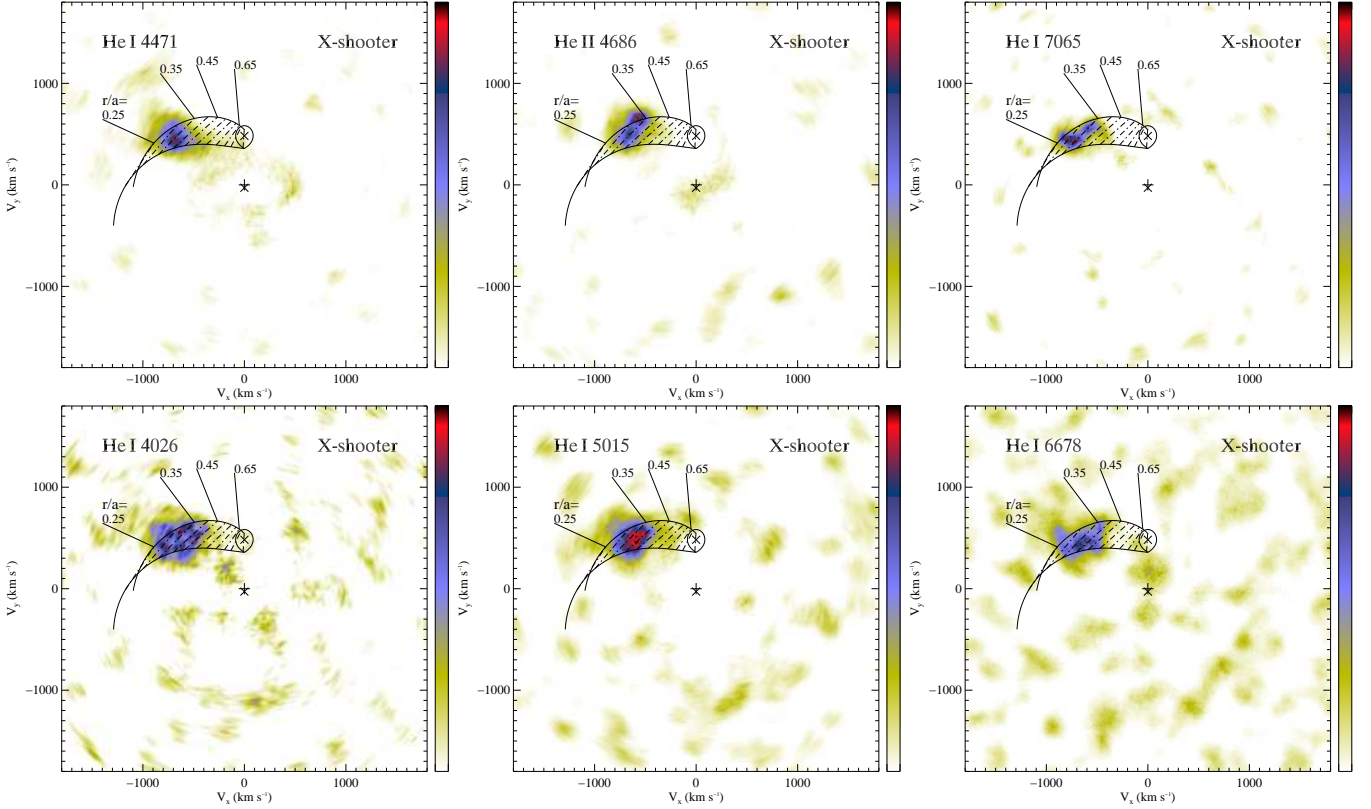


Figure 13. The Doppler maps of selected He I and He II lines.

evolution of the appearance of the hotspot area.¹¹ To this end, we

used shorter subsets of spectra¹² whose midphases vary from 0 to 1. A static version of the map in which the individual tomograms are centred around the hotspot area and scaled according to their mini-

¹¹ The animation may be viewed at <https://vitaly.neustroev.net/researchfiles/bwscl/>

¹² For this map, we used subsets of spectra consisting of 40 per cent of the whole X-shooter data set.

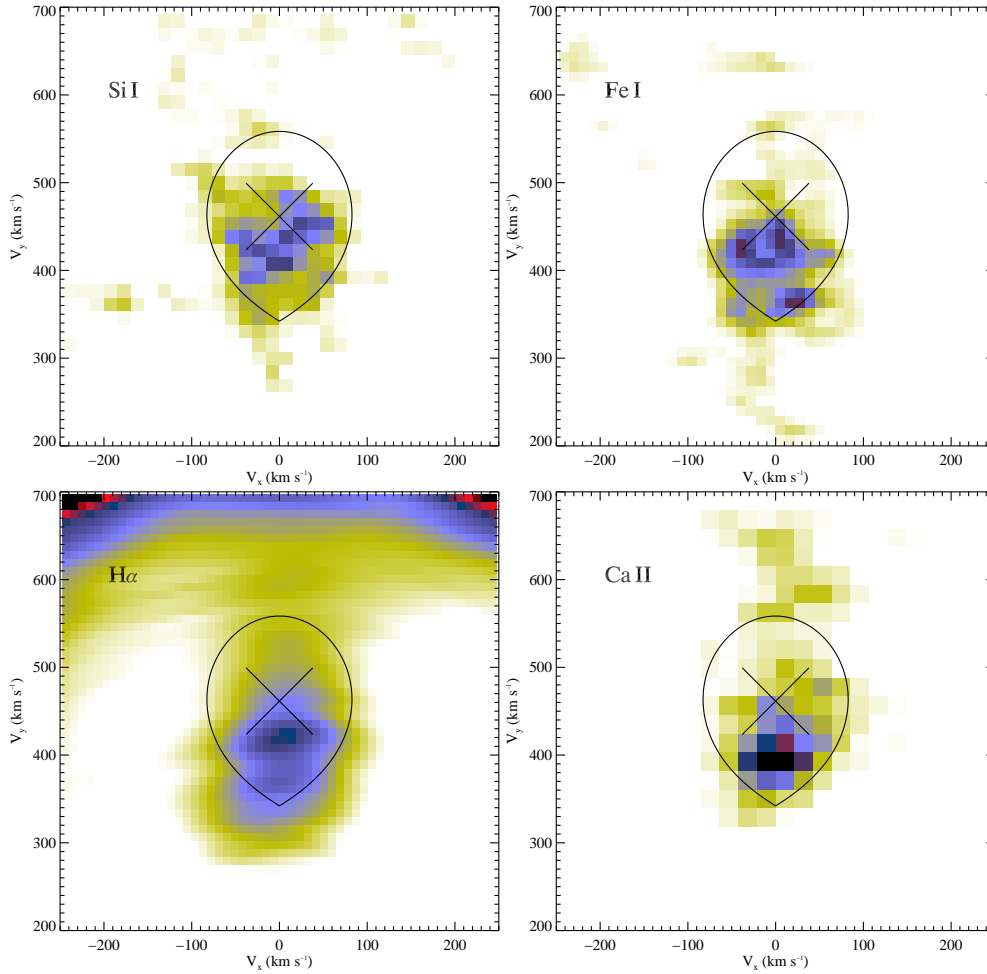


Figure 14. Zoomed parts of the tomograms of the lines in which the donor star is detected (Si I, Fe I, $H\alpha$, and Ca II). The maps are centred around the donor area.

imum and maximum values is shown in Figure 15. The full velocity range map scaled according to the average disc brightness can be found in Figure A6.

The trailed spectra of other than hydrogen lines do not show the S-wave splitting and shadow, although the disappearance of the S-wave at phase 0.6 can be detected in the strongest He I lines (Figure 12). As a result, the Doppler maps of these lines indicate at most only a weak presence of anisotropy of the hotspot emission. The hotspot area in the helium lines is much more compact than in the hydrogen lines (Figure 13), although the maximum of the helium emission is also located well inside the disc, at the same range of distances from the WD $r_{\text{hs}} \approx 0.35\text{--}0.40 a$. Similarly, a weak helium emission can also be traced along the stream until the disc edge at $\sim 0.6 a$. The He II 4686 Å line is very similar in appearance to the He I lines.

7 DISCUSSION

7.1 Evolutionary status of BW Scl

An accurate characterization of donor stars in short-period CVs (in particular, the measurement of their mass and effective temperature/spectral type) is a difficult task. This requires the combined use of different spectral lines that originated in the donor photosphere. These lines are usually very weak in the spectra of short-period CVs and can hardly be detected. The problem becomes even

more complex in the case of period-bouncers. The spectra of low-temperature donors in these systems, brown dwarf-like objects, peak in the NIR where obtaining high-quality spectra is challenging. As a result, only very few period-bounce candidates in quiescence revealed their donors in spectra (Harrison 2016, 2017; Pala et al. 2019, see also Littlefair et al. 2003 for discussion).

Dynamical information about the donor star can potentially be derived through the detection of irradiation-induced emission lines. Although such lines are usually detected in the spectra of longer period CVs (Harlaftis et al. 1999; Schwöpe et al. 2000), sometimes they are also seen in short-period dwarf novae during their superoutbursts and/or the following decline (Steehns et al. 2001). The latter becomes possible because of significant compressional heating of the WD during outbursts up to a few $\times 10^4$ K (see e.g. Long et al. 2003; Bullock et al. 2011). It is, however, generally accepted that after subsequent cooling and in proper quiescence the WDs in short-period CVs are not hot enough (the observed $T_{\text{eff}} \lesssim 15\,000$ K; Pala et al. 2017, 2022) to excite, at detectable levels, emission lines from the inner hemisphere of the donor star. Indeed, to the best of our knowledge, no such detections were reported to date.

Nevertheless, this study demonstrates that, at least under certain conditions, the irradiation-driven lines can be strong enough to be seen. These lines allowed us to make a good estimate for the radial velocity amplitude of the donor star in BW Scl and to derive accurate system parameters. The donor is found to have a mass of

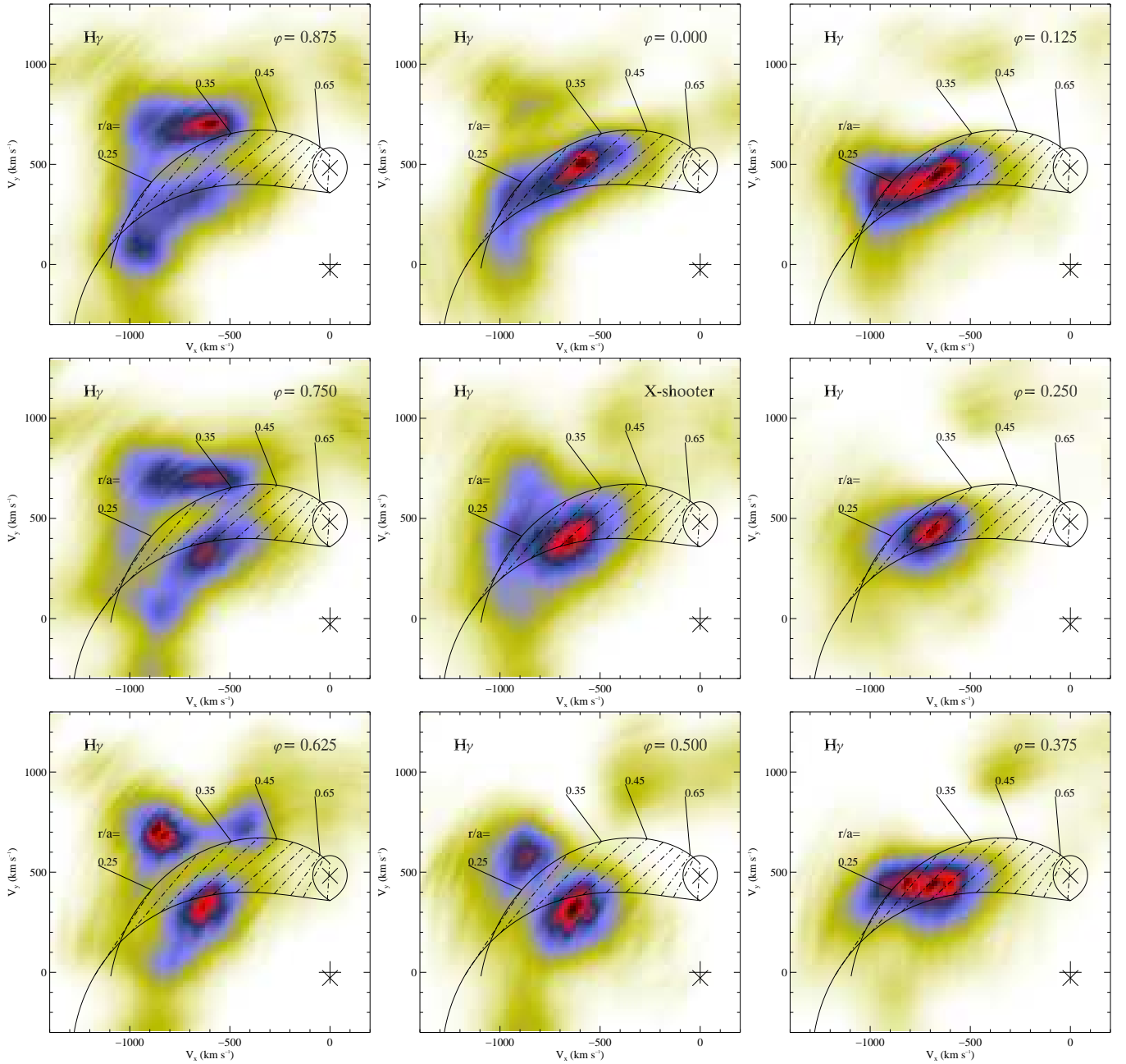


Figure 15. The evolution of the appearance of the hotspot area on Doppler maps of $H\gamma$, which were calculated using 40 per cent of spectra centred on phases shown on the maps. The central map was calculated using all the spectra. The maps are scaled according to their minimum and maximum values.

$0.051 \pm 0.006 M_{\odot}$ which is well below the hydrogen-burning limit.¹³ This indicates that BW Scl might have already evolved through the period minimum. Indeed, although the formal error of the M_2 estimate leaves room for different interpretations, a low temperature of the donor ($\lesssim 1600$ K) allows for further restricting its mass and the evolutionary status of the system. Figure 16 (right-hand

¹³ It is well known that the hydrogen-burning limit depends on metallicity (Chabrier & Baraffe 1997), with lower metallicity corresponding to a higher limit. Theoretically and empirically determined limits range from 0.070 to 0.08 M_{\odot} ; below 0.07 M_{\odot} , brown dwarfs never reach a steady state where they can fuse hydrogen (Fernandes et al. 2019; Forbes & Loeb 2019).

panel) shows a relation between the mass and temperature of the donor along the ‘standard’ and ‘best-fitting’ evolutionary tracks of CVs from Knigge et al. (2011). It is apparent from the figure that only a donor star that has passed the period minimum and that has a mass $\lesssim 0.052 M_{\odot}$ can have so low temperature. In more recent population synthesis studies, it has also been shown that T_{eff} of the donor after the period bounce is expected to be lower than ~ 2000 K (Goliasch & Nelson 2015), and that this bounce occurs at $M_2 \approx 0.07 M_{\odot}$ (Belloni et al. 2020). Empirically, using a large set of eclipsing CVs, McAllister et al. (2019) have shown that the bounce occurs at $P_{\text{min}} = 76.3 \pm 1.0$ min and $M_2 = 0.063^{+0.005}_{-0.002} M_{\odot}$. In the $P_{\text{orb}} - M_2$ and $T_{\text{eff},2} - M_2$ diagrams (Figure 16), BW Scl is located be-

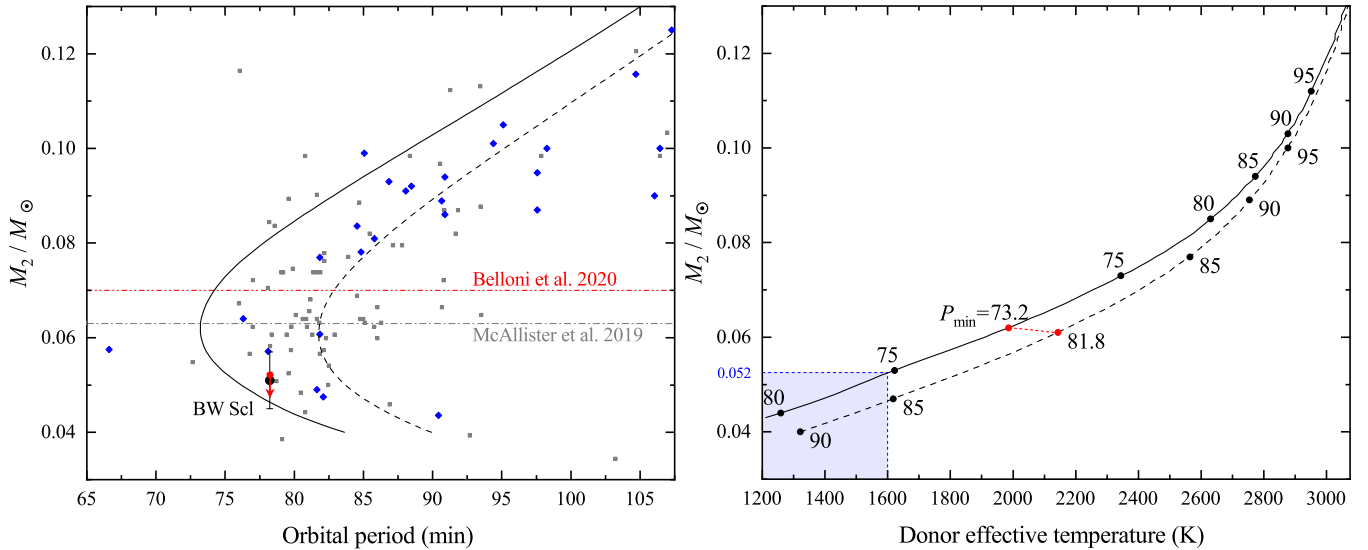


Figure 16. Left: donor masses in short-period CVs versus orbital periods. The large black dot with error bars represents a dynamically measured donor mass in BW Scl, whereas the red dot with an arrow shows the upper limit of the mass estimated from the donor temperature. The blue and grey points represent masses determined by eclipse modelling from [McAllister et al. \(2019\)](#) and the stage A superhump method ([Kato 2022](#)), for which error bars have been omitted for clarity. The two horizontal lines indicate the donor mass at which the period bounce occurs, according to [McAllister et al. \(2019\)](#) and [Belloni et al. \(2020\)](#). Right: donor masses versus donor temperatures in short-period CVs. The black solid and dashed lines represent the ‘optimal’ and ‘standard’ evolutionary tracks from [Knigge et al. \(2011\)](#), respectively; the red dotted line connects P_{min} in these tracks. The dashed blue lines and shaded region show the range of masses for a donor with $T_{\text{eff},2} \leq 1600$ K.

low the turning point and, therefore, its donor is a sub-stellar object. Thus, although from the P_{orb} only it is difficult to assess the evolutionary status of BW Scl because it is located near the theoretical P_{min} , all the above arguments indicate that the system has already passed it and started moving toward longer periods.

A possible period-bouncer status of BW Scl has been questioned by [Pala et al. \(2022\)](#). They argue that the measured T_{eff} of its WD is inconsistent with the theoretical predictions for period bouncers and must be $\lesssim 12\,500$ K. Since \dot{M} is expected to drop as a CV passes beyond P_{min} ([Knigge et al. 2011](#); [Goliash & Nelson 2015](#); [Belloni et al. 2020](#)), T_{eff} should also fall as it is set by the compressional heating of the accreted material ([Townesley & Bildsten 2004](#)). When T_{eff} is measured in quiescence, it provides a constraint on the mean mass-accretion rate $\langle \dot{M} \rangle$ averaged over the thermal time-scale of the WD envelope ($\sim 10^5$ yr). For BW Scl with $T_{\text{eff}} = 14\,250$ K and $M_{\text{wd}} = 0.85 M_\odot$, equation 2 in [Townesley & Gänsicke \(2009\)](#) gives $\langle \dot{M} \rangle = 6.2 \times 10^{-11} M_\odot/\text{yr}$, whereas the most recent population synthesis study by [Belloni et al. \(2020, fig. 4\)](#) predicts the range of \dot{M} at P_{min} to be $(6.3\text{--}8.8) \times 10^{-11} M_\odot/\text{yr}$. Thus, both the measured T_{eff} and calculated $\langle \dot{M} \rangle$ are in general agreement with the theory, but, together with other parameters, testify that BW Scl is still at the very beginning of its post- P_{min} evolution.

7.2 Optically thin accretion disc

Accretion discs in CVs with low-mass accretion rates have outer regions optically thin in continuum ([Williams 1980](#)). [Tylenda \(1981\)](#) has shown that when lowering \dot{M}_{acc} , the outer optically thin region of the disc extends down to its inner edge (the WD surface), and at $\dot{M}_{\text{acc}} \approx 5 \times 10^{13} \text{ g s}^{-1}$ the entire disc becomes optically thin in continuum. The observed \dot{M}_{acc} in BW Scl is lower than the above limit implying that most of its accretion disc, possibly the entire disc is optically thin. As a simple exercise, we can estimate the mean effective

(blackbody) temperature of the disc using the definition of the luminosity as the integral of the total flux over the disc surface:

$$L_d = 2\pi r_d^2 \sigma T_{\text{eff}}^4, \quad (14)$$

where σ is the Stefan–Boltzmann constant, $r_d = r_{d,\text{max}}$ is the disc radius, and the factor 2 represents the radiation from the two sides of the disc. For $L_d \lesssim 3.2 \times 10^{30} \text{ erg s}^{-1}$ and $r_{d,\text{max}} = 0.338 R_\odot$ we obtain T_{eff} to be very low, ~ 2000 K. It is unlikely that so low blackbody temperature represents the true, kinetic temperature of the disc material as the latter has to be heated up by e.g. viscosity ([Williams 1980](#); [Tylenda 1981](#)). This additionally supports the optically thin conditions in the disc of BW Scl. However, the found flat Balmer decrement of the disc ([Table 6](#)) is indicative of optically thick emission in Balmer lines which are excited rather collisionally than being produced via photoionization. It suggests that despite the relatively strong irradiating flux from the WD which is able to produce emission lines from the donor star, yet it is not strong enough to have produced the emission lines from the disc by photoionization alone.

The measured parameters of the Balmer lines can give us some idea of the temperature and density of the line emitting regions. Comparing the observed Balmer decrements and the EWs of BW Scl with the model predictions calculated by [Williams \(1991\)](#), we find that they are roughly consistent with the disc temperature in the range of 10 000–15 000 K and the number density of hydrogen at the mid-plane of $\log N_0 \approx 12$. However, Williams’ radiative transfer models predict much lower EWs than we observe in BW Scl, pointing to an even lower density.

There is another, although indirect, evidence for a low-density outer regions of the disc in BW Scl. It has been shown for several short-period CVs (WZ Sge; [Skidmore et al. 2000](#); [Mason et al. 2000](#); HT Cas; [Neustroev et al. 2016](#); [Neustroev & Zharikov 2020](#); EZ Lyn; [Amantayeva et al. 2021](#)) that the position of the hotspot in their discs is consistent with the trajectory of the gas stream but is

located much closer to the WD than the disc edge. It is interesting to note that the radial location of the hotspot in those systems is roughly consistent with the circularization radius R_{circ} . In this work we show that this also seems to be correct for BW Scl, for which $R_{\text{circ}}=0.39a$ (for $q=0.060$) appears to be very close to $r_{\text{hs}}\approx 0.35\text{--}0.40a$ (Section 6.3). Moreover, the Doppler maps of BW Scl show how the stream propagates through the disc from its very edge to the hotspot. This structure resembles the so-called hot line, first predicted by Bisikalo et al. (1998). Their numerical simulations show that if the gas stream is denser than the outer disc then the stream will be able to flow all the way down to the inner disc regions, forming an extended shock wave along the ballistic trajectory.

7.3 Optically thick hotspot and double-wave modulations

The origin of double-wave modulations which are frequently observed in light curves of short-period CVs in quiescence is still under debate, but it is generally accepted that they are associated with some structures in the accretion disc. In BW Scl, the disc contributes ~ 40 per cent to the total light (in the *TESS* bandpass, Section 6.2) which is modulated with the total amplitude of ~ 8 per cent (Section 3.1). Thus, these structures are accounted for ~ 20 per cent of the accretion disc variability. Two possible interpretations have been suggested to explain this phenomenon.

The first one attributes a double-wave light curve to changing viewing aspect of the optically thick hotspot shining through/above an optically thin accretion disc (Robinson et al. 1978; Spruit & Rutten 1998; Skidmore et al. 2000). This seems to be in accordance with our results. An almost transparent disc as it is seen in BW Scl allows the light from the elongated hotspot to escape in all directions, while the variable aspect of the hotspot modulates the observed flux. We point out that one of the light maxima in BW Scl occurs at spectroscopic phase 0.86, which is consistent with the phase of maximum of an orbital hump from the stream-disc collision, typically observed in high-inclination CVs (Warner 1995).

Another interpretation involves spiral arm structures in the disc which appear due to the 2:1 resonance (Zharikov et al. 2008). In a recent work, Amantayeva et al. (2021) have reported a study of EZ Lyn, another period-bouncer having many properties similar to BW Scl. Amantayeva et al. claim that they were able to successfully reproduce the double-wave light curve of EZ Lyn, using a model that includes an accretion disc with a spiral pattern.¹⁴ Nevertheless, besides a broader question of the appearance of the spirals in the disc, we have other reasons to doubt this interpretation. In order for double-wave modulations to occur, the spiral structure must be optically thick in the optical light. However, the blackbody temperature of the continuum-forming region in EZ Lyn was found to be only 1200–1800 K, while a temperature excess of the spirals (in percent from the disc temperature) is just ~ 31 per cent. These results indicate that the spirals should they exist are also optically thin and thus unable to modulate the observed flux; still, they are treated as optically thick in the mentioned work. Finally, even assuming that the proposed spirals can modulate the flux, they should manifest themselves in spectral lines, but the very high-quality Doppler maps of BW Scl show no sign of them. Instead, the maps display only the bright, optically thick elongated hotspot (hot line), which cannot help but modulate the signal. Thus, our data do not support the attribution of double-wave modulations to spiral structures in the disc.

8 SUMMARY

We have analysed multi-epoch spectroscopic and photometric observations of the WZ Sge-type dwarf nova BW Scl, a period-bouncer candidate. The time-resolved spectroscopic data were obtained in quiescence in 2001, 2002, 2010, 2017 and 2018, before and after the 2011 superoutburst. High-cadence (1 min) X-shooter spectra allowed us to detect multiple irradiation-induced emission lines from the donor star, permitting the radial velocity variations to be measured with high accuracy. Using the Mg II 4481 Å and Ca II K absorption lines originated in the photosphere of the accreting WD, we measured its radial velocities and the gravitational redshift, allowing direct measurement of the WD mass. The most important results of this study can be summarized as follows

- (i) We derived the orbital ephemeris of BW Scl combining *TESS* and AAVSO photometry and X-shooter spectroscopy.
- (ii) The WD in BW Scl has a mass of $M_{\text{wd}}=0.85\pm 0.04 M_{\odot}$.
- (iii) The measured WD temperature is 14250 K.
- (iv) The donor is a sub-stellar object with $M_2=0.051\pm 0.006 M_{\odot}$, well below the hydrogen-burning limit.
- (v) Combined NIR spectra, Doppler-corrected into the frame of the donor star, show the K I 12432 and 12522 Å absorption lines and hints of a few other species which are expected to be seen in spectra of L and T brown dwarfs. However, their presence should be confirmed in further studies.
- (vi) Using NIR photometric and spectroscopic data, we put a conservative upper limit on the effective temperature of the donor to be $T_{\text{eff}} \leq 1600$ K, corresponding to a brown dwarf of T spectral type.
- (vii) The accretion disc in BW Scl has a very low luminosity $L_{\text{d}} \lesssim 4 \times 10^{30} \text{ erg s}^{-1}$ which corresponds to a very low mass accretion rate of $\dot{M}_{\text{acc}} \lesssim 7 \times 10^{-13} M_{\odot} \text{ yr}^{-1}$. We show that such a disc is optically thin in continuum but optically thick in Balmer lines.
- (viii) The outer parts of the disc have a low density allowing the stream to flow down to the inner disc regions. The brightest part of the hotspot is located close to the circularization radius of the disc. The hotspot is optically thick and has a complex, elongated structure.
- (ix) We suggest that double-wave modulations seen in the light curve of BW Scl and similar objects are produced due changing viewing aspect of the optically thick hotspot shining through an optically thin accretion disc.
- (x) Although the measured donor parameters are consistent with that BW Scl has already passed the minimum period and started moving toward longer periods, the relatively high WD temperature indicates that the system is still at the very beginning of its post- P_{min} evolution.

In conclusion, we note that the spectra of BW Scl demonstrate a wealth of features that allow studying this object in great detail, permitting us to name this object ‘a treasure chest’ of accreting WDs. Unfortunately, our NIR spectra are not good enough to investigate the properties of the donor. Accurate measurement of its parameters is of the highest importance as the current theory is not able to predict physical properties of such a kind of brown dwarf-like objects with high precision (Knigge et al. 2011). BW Scl is bright enough to allow obtaining deeper NIR spectra than we currently have.

ACKNOWLEDGEMENTS

We would like to thank the anonymous referee for useful comments. VN acknowledges the financial support from the visitor and mobility program of the Finnish Centre for Astronomy with ESO (FINCA),

¹⁴ Besides a disc with two spirals, this multicomponent model includes two extended spots at the outer edge of the disc.

funded by the Academy of Finland grant nr 306531. Based on observations made with ESO Telescopes at the La Silla Paranal Observatory under programme IDs 068.D-0153, 069.D-0391, 086.D-0775, 100.D-0932, and 101.D-0806. This paper includes data collected by the *TESS* mission, which are publicly available from the Mikulski Archive for Space Telescopes (MAST). Funding for the *TESS* mission is provided by the NASA's Science Mission Directorate. This publication makes use of data products from the *Wide-field Infrared Survey Explorer*, which is a joint project of the University of California, Los Angeles, and the Jet Propulsion Laboratory/California Institute of Technology, funded by the National Aeronautics and Space Administration. This publication also makes use of data products from NEOWISE, which is a project of the Jet Propulsion Laboratory/California Institute of Technology, funded by the Planetary Science Division of the National Aeronautics and Space Administration. This research made use of StarCAT, hosted by the MAST. STScI is operated by the Association of Universities for Research in Astronomy, Inc., under NASA contract NAS5-26555. We thank the *Swift* PI, Brad Cenko, for approving the observations, and the *Swift* planning and operations teams for their ongoing support. We acknowledge with thanks the variable star observations from the *AAVSO International Data base* contributed by observers worldwide and used in this research.

DATA AVAILABILITY

The observational data used in this paper are publicly available in the ESO¹⁵, NASA/IPAC¹⁶, MAST¹⁷, and HEASARC¹⁸ archives.

References

- Abbott T. M. C., Fleming T. A., Pasquini L., 1997, *A&A*, **318**, 134
- Amantayeva A., Zharikov S., Page K. L., Pavlenko E., Sosnovskij A., Khokhlov S., Ibraimov M., 2021, *ApJ*, **918**, 58
- Augustejn T., Wisotzki L., 1997, *A&A*, **324**, L57
- Ayres T. R., 2010, *ApJS*, **187**, 149
- Bailer-Jones C. A. L., Rybizki J., Fouesneau M., Demleitner M., Andrae R., 2021, *AJ*, **161**, 147
- Bédard A., Bergeron P., Brassard P., Fontaine G., 2020, *ApJ*, **901**, 93
- Belloni D., Schreiber M. R., Pala A. F., Gänsicke B. T., Zorotovic M., Rodríguez C. V., 2020, *MNRAS*, **491**, 5717
- Bisikalo D. V., Boyarchuk A. A., Chechetkin V. M., Kuznetsov O. A., Molteni D., 1998, *MNRAS*, **300**, 39
- Bullock E., et al., 2011, *AJ*, **141**, 84
- Burrows D. N., et al., 2005, *Space Sci. Rev.*, **120**, 165
- Buzzoni B., et al., 1984, *The Messenger*, **38**, 9
- Cannizzo J. K., 1993, in , *Accretion Disks in Compact Stellar Systems*. pp 6–40, doi:10.1142/9789814350976_0002
- Chabrier G., Baraffe I., 1997, *A&A*, **327**, 1039
- Claret A., Cukanovaite E., Burdge K., Tremblay P. E., Parsons S., Marsh T. R., 2020, *A&A*, **634**, A93
- Cook M. C., Warner B., 1984, *MNRAS*, **207**, 705
- Cutri R. M., et al., 2003, *VizieR Online Data Catalog*, p. II/246
- Czesla S., Schröter S., Schneider C. P., Huber K. F., Pfeifer F., Andreasen D. T., Zechmeister M., 2019, *PyA: Python astronomy-related packages*, *Astrophysics Source Code Library*, record ascl:1906.010 (ascl:1906.010)
- Dekker H., D’Odorico S., Kaufer A., Delabre B., Kotzlowski H., 2000, in Iye M., Moorwood A. F., eds, *Society of Photo-Optical Instrumentation Engineers (SPIE) Conference Series Vol. 4008, Optical and IR Telescope Instrumentation and Detectors*. pp 534–545, doi:10.1117/12.395512
- Drake A. J., et al., 2009, *ApJ*, **696**, 870
- Fernandes C. S., Van Grootel V., Salmon S. J. A. J., Aringer B., Burgasser A. J., Scufflaire R., Brassard P., Fontaine G., 2019, *ApJ*, **879**, 94
- Forbes J. C., Loeb A., 2019, *ApJ*, **871**, 227
- Freudling W., Romaniello M., Bramich D. M., Ballester P., Forchi V., García-Dabó C. E., Moehler S., Neeser M. J., 2013, *A&A*, **559**, A96
- Friend M. T., Martin J. S., Smith R. C., Jones D. H. P., 1988, *MNRAS*, **233**, 451
- Gaia Collaboration et al., 2021, *A&A*, **649**, A1
- Gänsicke B. T., Szkody P., Howell S. B., Sion E. M., 2005, *ApJ*, **629**, 451
- Gehrels N., et al., 2004, *ApJ*, **611**, 1005
- Goliash J., Nelson L., 2015, *ApJ*, **809**, 80
- Greenstein J. L., Trimble V. L., 1967, *ApJ*, **149**, 283
- Harlaftis E. T., Steeghs D., Horne K., Martín E., Magazzú A., 1999, *MNRAS*, **306**, 348
- Harrison T. E., 2016, *ApJ*, **816**, 4
- Harrison T. E., 2017, *PASP*, **129**, 124203
- Hayashi C., Nakano T., 1963, *Progress of Theoretical Physics*, **30**, 460
- Hedemäki J., 2021, Master’s Thesis, University of Oulu, <http://urn.fi/URN:NBN:fi:oulu-202108048811>
- Hernández Santisteban J. V., et al., 2016, *Nature*, **533**, 366
- Holberg J. B., Barstow M. A., Green E. M., 1997, *ApJ*, **474**, L127
- Howell S. B., Rappaport S., Politano M., 1997, *MNRAS*, **287**, 929
- Howell S. B., Nelson L. A., Rappaport S., 2001, *ApJ*, **550**, 897
- Jayasinghe T., et al., 2021, *MNRAS*, **503**, 200
- Kato T., 2015, *PASJ*, **67**, 108
- Kato T., 2022, arXiv e-prints, p. arXiv:2201.02945
- Kato T., Osaki Y., 2013, *PASJ*, **65**, 115
- Kato T., et al., 2013, *PASJ*, **65**, 23
- Kausch W., et al., 2015, *A&A*, **576**, A78
- Kepler S. O., Kleinman S. J., Nitta A., Koester D., Castanheira B. G., Giovannini O., Costa A. F. M., Althaus L., 2007, *MNRAS*, **375**, 1315
- Kimura M., et al., 2018, *PASJ*, **70**, 47
- Knigge C., Baraffe I., Patterson J., 2011, *ApJS*, **194**, 28
- Koester D., 2010, *Mem. Soc. Astron. Italiana*, **81**, 921
- Kolb U., 1993, *A&A*, **271**, 149
- Korn A. J., Grundahl F., Richard O., Mashonkina L., Barklem P. S., Collet R., Gustafsson B., Piskunov N., 2007, *ApJ*, **671**, 402
- Kumar S. S., 1963, *ApJ*, **137**, 1121
- Lallement R., et al., 2018, *A&A*, **616**, A132
- Larsen S. S., Richtler T., 2006, *A&A*, **459**, 103
- Littlefair S. P., Dhillon V. S., Martín E. L., 2003, *MNRAS*, **340**, 264
- Long K. S., Froning C. S., Gänsicke B., Knigge C., Sion E. M., Szkody P., 2003, *ApJ*, **591**, 1172
- Ludwig K., Meyer-Hofmeister E., Ritter H., 1994, *A&A*, **290**, 473
- Mainzer A., et al., 2011, *ApJ*, **731**, 53
- Mainzer A., et al., 2014, *ApJ*, **792**, 30
- Marsh T. R., 2001, in Boffin H. M. J., Steeghs D., Cuypers J., eds, , Vol. 573, *Astrotromography, Indirect Imaging Methods in Observational Astronomy*. p. 1
- Marsh T. R., Horne K., 1988, *MNRAS*, **235**, 269
- Mason E., Skidmore W., Howell S. B., Ciardi D. R., Littlefair S., Dhillon V. S., 2000, *MNRAS*, **318**, 440
- McAllister M., et al., 2019, *MNRAS*, **486**, 5535
- Mennickent R. E., Diaz M. P., Tappert C., 2004, *MNRAS*, **347**, 1180
- Million C., et al., 2016, *ApJ*, **833**, 292
- Moorwood A., Cuby J. G., Lidman C., 1998, *The Messenger*, **91**, 9
- Nauenberg M., 1972, *ApJ*, **175**, 417
- Neustroev V. V., Zharikov S., 2008, *MNRAS*, **386**, 1366
- Neustroev V. V., Zharikov S. V., 2020, *A&A*, **642**, A100
- Neustroev V. V., Zharikov S. V., Borisov N. V., 2016, *A&A*, **586**, A10
- Neustroev V. V., et al., 2017, *MNRAS*, **467**, 597
- Neustroev V., Knigge C., Zharikov S., 2018a, in *Proceedings of The Golden Age of Cataclysmic Variables and Related Objects IV — PoS(GOLDEN*

¹⁵ <http://archive.eso.org>

¹⁶ <https://irsa.ipac.caltech.edu>

¹⁷ <https://mast.stsci.edu>

¹⁸ <https://heasarc.gsfc.nasa.gov/docs/archive.html>

- 2017). p. 034, doi:[10.22323/1.315.0034](https://doi.org/10.22323/1.315.0034)
- Neustroev V. V., et al., 2018b, *A&A*, **611**, [A13](#)
- Pala A. F., et al., 2017, *MNRAS*, **466**, [2855](#)
- Pala A. F., Schmidtobreick L., Tappert C., Gänsicke B. T., Mehner A., 2018, *MNRAS*, **481**, [2523](#)
- Pala A. F., et al., 2019, *MNRAS*, **483**, [1080](#)
- Pala A. F., et al., 2022, *MNRAS*, **510**, [6110](#)
- Parsons S. G., Marsh T. R., Copperwheat C. M., Dhillon V. S., Littlefair S. P., Gänsicke B. T., Hickman R., 2010, *MNRAS*, **402**, [2591](#)
- Parsons S. G., Marsh T. R., Gänsicke B. T., Tappert C., 2011, *MNRAS*, **412**, [2563](#)
- Parsons S. G., et al., 2012, *MNRAS*, **420**, [3281](#)
- Patterson J., 2011, *MNRAS*, **411**, [2695](#)
- Reis R. C., Wheatley P. J., Gänsicke B. T., Osborne J. P., 2013, *MNRAS*, **430**, [1994](#)
- Robinson E. L., Nather R. E., Patterson J., 1978, *ApJ*, **219**, [168](#)
- Romero A. D., Kepler S. O., Joyce S. R. G., Lauffer G. R., Córscico A. H., 2019, *MNRAS*, **484**, [2711](#)
- Roming P. W. A., et al., 2005, *Space Sci. Rev.*, **120**, [95](#)
- Schreiber M. R., Zorotovic M., Wijnen T. P. G., 2016, *MNRAS*, **455**, [L16](#)
- Schwope A. D., Catalán M. S., Beuermann K., Metzner A., Smith R. C., Steeghs D., 2000, *MNRAS*, **313**, [533](#)
- Shanks T., et al., 2015, *MNRAS*, **451**, [4238](#)
- Shappee B. J., et al., 2014, *ApJ*, **788**, [48](#)
- Sion E. M., Godon P., 2022, *Galaxies*, **10**, [43](#)
- Skidmore W., Mason E., Howell S. B., Ciardi D. R., Littlefair S., Dhillon V. S., 2000, *MNRAS*, **318**, [429](#)
- Smartt S. J., et al., 2015, *A&A*, **579**, [A40](#)
- Smette A., et al., 2015, *A&A*, **576**, [A77](#)
- Spitzer Science Center S., Infrared Science Archive I., 2021, VizieR Online Data Catalog, [p. II/368](#)
- Spruit H. C., 1998, arXiv e-prints, [pp astro-ph/9806141](#)
- Spruit H. C., Rutten R. G. M., 1998, *MNRAS*, **299**, [768](#)
- Steeghs D., Marsh T., Knigge C., Maxted P. F. L., Kuulkers E., Skidmore W., 2001, *ApJ*, **562**, [L145](#)
- Townsley D. M., Bildsten L., 2004, *ApJ*, **600**, [390](#)
- Townsley D. M., Gänsicke B. T., 2009, *ApJ*, **693**, [1007](#)
- Tylenda R., 1981, *Acta Astron.*, **31**, [127](#)
- Uthas H., et al., 2012, *MNRAS*, **420**, [379](#)
- Vernet J., et al., 2011, *A&A*, **536**, [A105](#)
- Wade R. A., Horne K., 1988, *ApJ*, **324**, [411](#)
- Warner B., 1995, *Cataclysmic Variable Stars*. Cambridge Astrophysics, Cambridge University Press, doi:[10.1017/CBO9780511586491](https://doi.org/10.1017/CBO9780511586491)
- Williams R. E., 1980, *ApJ*, **235**, [939](#)
- Williams G. A., 1991, *AJ*, **101**, [1929](#)
- Wright E. L., et al., 2010, *AJ*, **140**, [1868](#)
- Zharikov S. V., et al., 2008, *A&A*, **486**, [505](#)
- Zorotovic M., Schreiber M. R., Gänsicke B. T., 2011, *A&A*, **536**, [A42](#)
- van Spaandonk L., Steeghs D., Marsh T. R., Parsons S. G., 2010, *ApJ*, **715**, [L109](#)

APPENDIX A: SUPPLEMENTARY FIGURES

This paper has been typeset from a \LaTeX file prepared by the author.

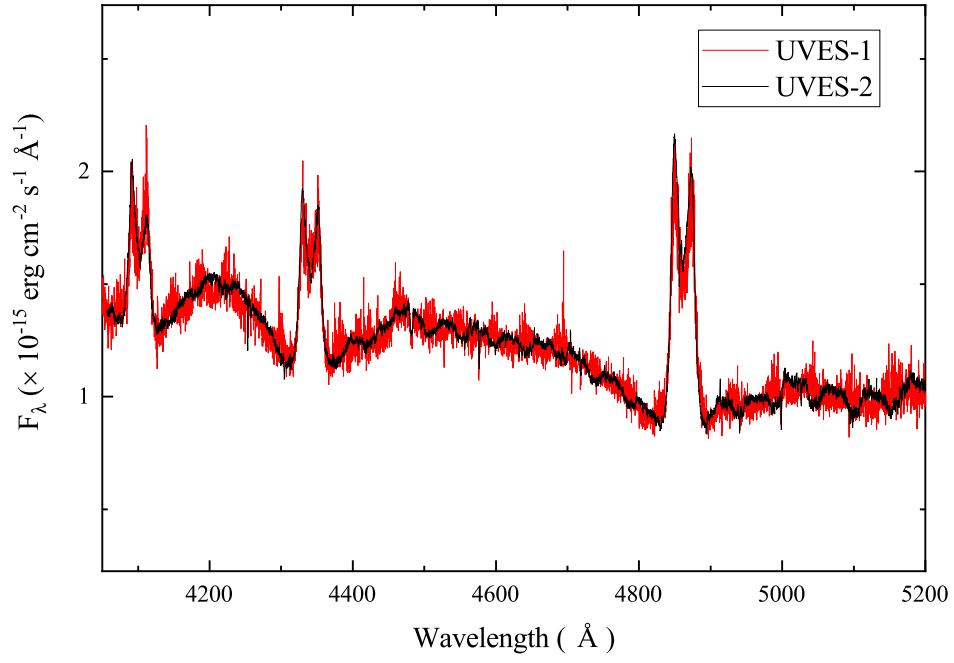


Figure A1. The mean UVES spectra clearly exhibit the Échelle order pattern.

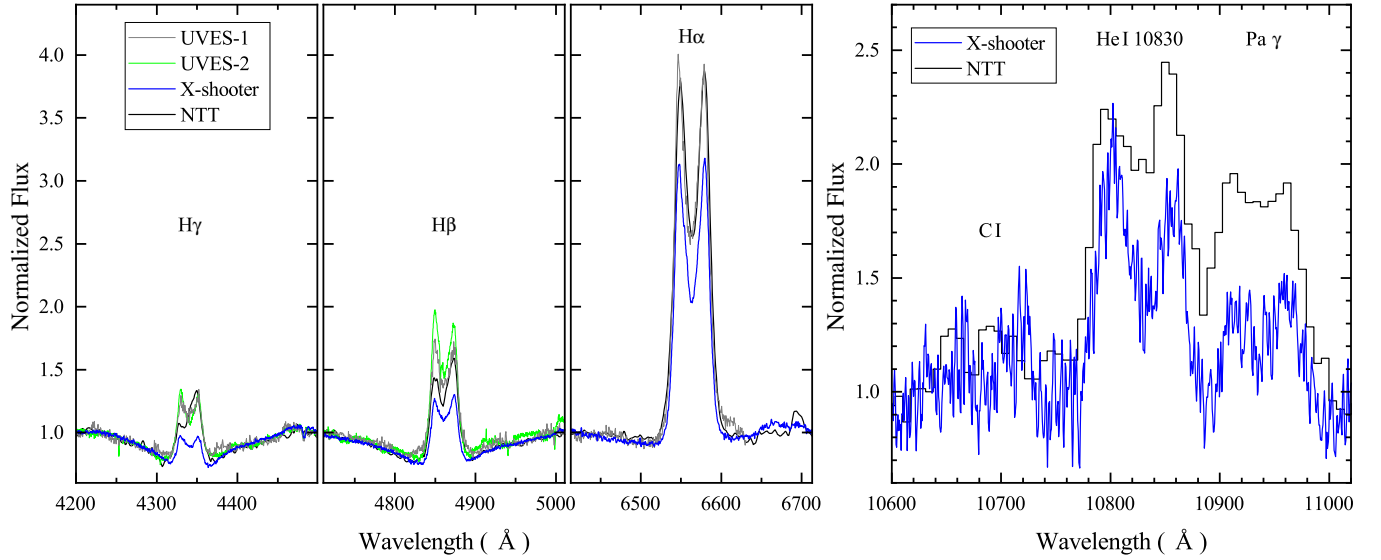


Figure A2. $H\alpha$, $H\beta$, and $H\gamma$ line profiles (left) and the region around the C I 10693 / He I 10830 / Pa γ complex (right) as seen in different data sets.

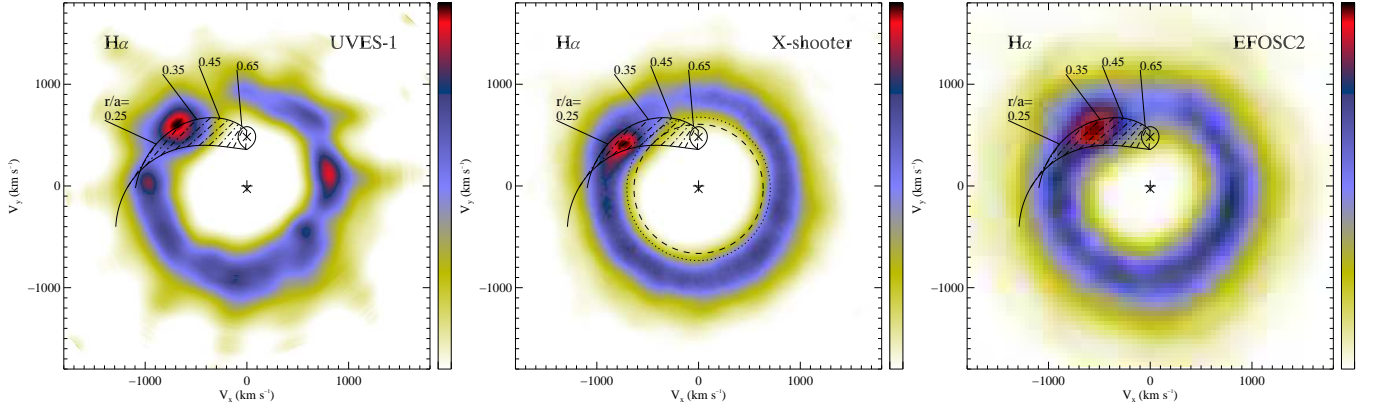


Figure A3. The Doppler maps of $H\alpha$ calculated using different data sets.

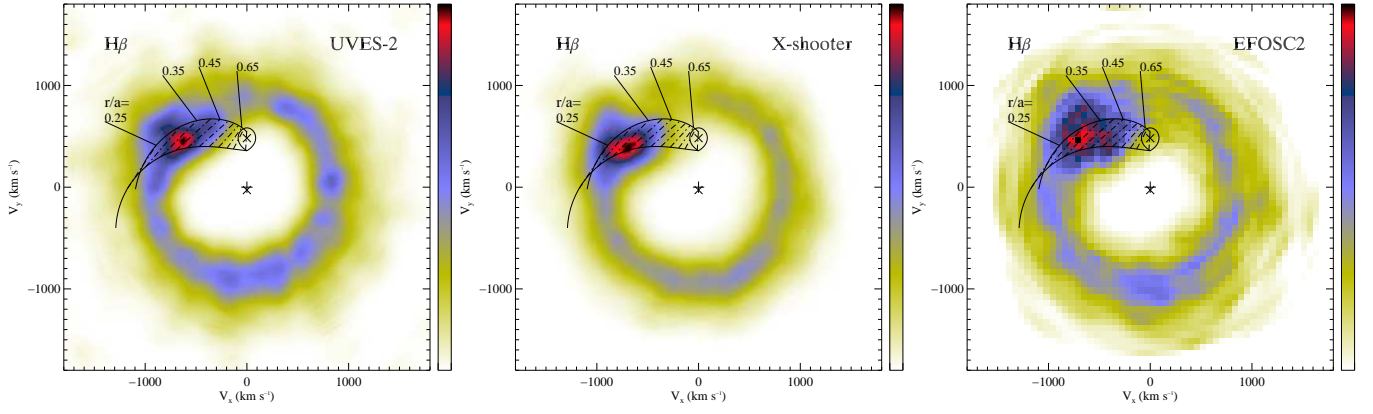


Figure A4. The Doppler maps of $H\beta$ calculated using different data sets.

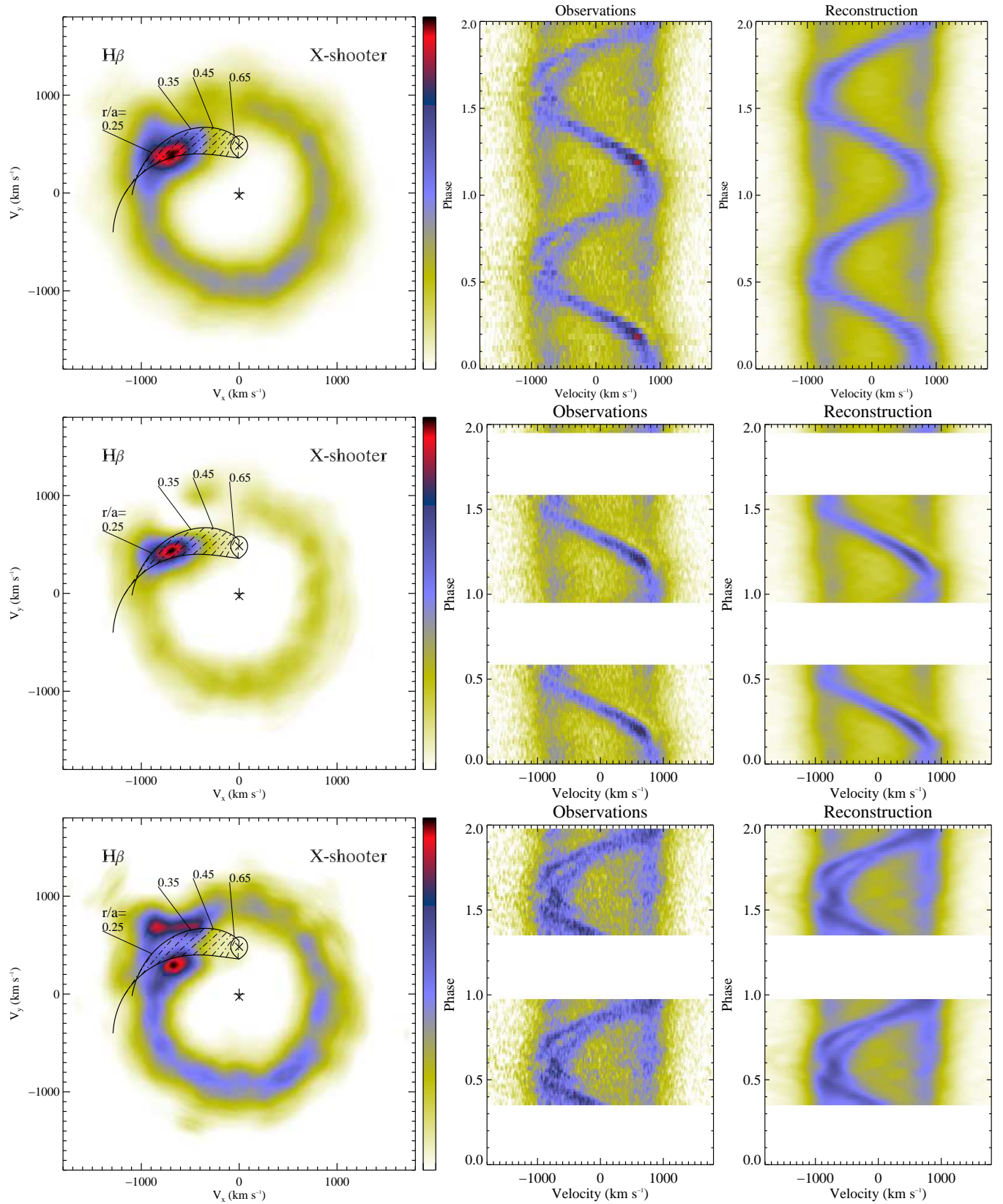


Figure A5. Same as Figure 10, for H β . The middle and lower maps were calculated using 60 per cent of the spectra centred on phases 0.25 and 0.65, respectively.

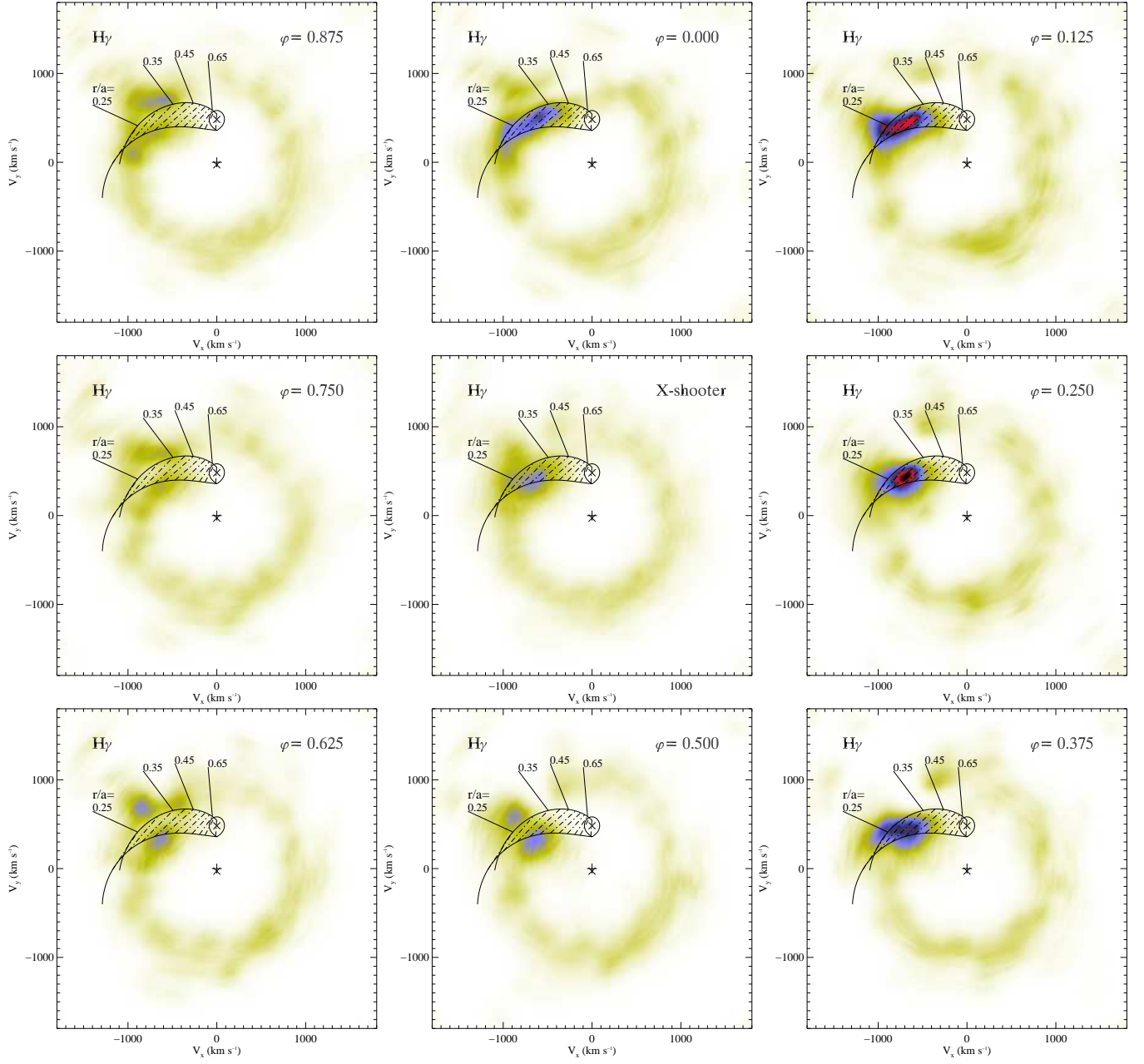


Figure A6. Same as [Figure 15](#), but the full velocity range maps were scaled according to the average disc brightness.